

ANALYSIS OF ADVANCED CONTROL ALGORITHMS AND STUDIES ON
SENSOR TECHNOLOGIES FOR EMULSION POLYMERIZATION CONTROL

By

BRIAN JOSEPH REMARK

A DISSERTATION PRESENTED TO THE GRADUATE SCHOOL
OF THE UNIVERSITY OF FLORIDA IN PARTIAL FULFILLMENT
OF THE REQUIREMENTS FOR THE DEGREE OF
DOCTOR OF PHILOSOPHY

UNIVERSITY OF FLORIDA

2004

To my parents, who always thought I was a professional student.

ACKNOWLEDGMENTS

I would like to express my sincere appreciation to my advisor, Oscar Crisalle, without whose support this dissertation would not have been possible. He gave me the freedom to work on my own.

I wish to thank Professors Jason Weaver, Richard Dickinson, and Haniph Latchman for serving on my supervisory committee. Between Dr. Latchman and Dr. Crisalle, they always knew the answer to my question.

I thank Jon Engelstad, Serkan Kincal, Chris Meredith, Ryan Acher, Ryan Kaczynski, Ricardo Gomez-Gonzalez, and especially Chuck Baab, who answered all of my unintelligent questions. They all have not only contributed greatly to my research but have been good friends.

Finally, I wish to thank my mom and dad and Heather for their unending support.

TABLE OF CONTENTS

page

ACKNOWLEDGMENTS	III
ABSTRACT	VII
CHAPTER	
1 INTRODUCTION	1
1.1. Motivation.....	1
1.2. Objective and Structure of Dissertation.....	3
2 COMPUTATION OF THE NONLINEAR NYQUIST ROBUST STABILITY MARGIN FOR UNCERTAIN SYSTEMS	5
2.1. Introduction.....	5
2.2. Generalization of the Critical Direction Theory	5
2.2.1. Preliminaries	5
2.2.2. Brief review of the Critical Direction Theory.....	6
2.2.3. Brief review of the Describing Function Method	8
2.3. Critical Direction Theory for Nonlinear Systems	9
2.4. Special Cases Under Consideration.....	15
2.4.1. Derivations Using Circular Value Sets	15
2.4.2. Real Affine Parametric Uncertainty.....	22
2.5. Examples.....	26
2.5.1. Circular Value Set with Simple Describing Function.....	26
2.5.2. Circular Value Set with Saturation Describing Function	29
2.5.3. Affine Uncertainty Structure with Describing Function.....	31
2.6. Conclusions and Future Work	33
3 SYSTEMATIC ALGORITHMS FOR CHARACTERIZING THE ROBUSTNESS OF PREDICTIVE CONTROLLERS	35
3.1. Introduction.....	35
3.2. Formulation of the Problem.....	37
3.2.1. Uncertainty Description	37
3.2.2. Robustness of Predictive Control Designs.....	39
3.3. Computation of the Parametric Stability Margin.....	42
3.3.1. Ellipsoidal Uncertainty	43

3.3.2. Hyperbox Uncertainty.....	45
3.4. Robustification of Predictive Controllers	45
3.4.1. Ellipsoidal Uncertainty.	46
3.4.2. Hyperbox Uncertainty.....	49
3.5. Conclusions.....	53
 4 PREDICTIVE CONTROL OF A WASTERWATER TREATMENT PLANT	54
4.1. Introduction.....	54
4.2. Derivation of Disturbance Predictive Controller.....	56
4.3. Simulation of Wastewater Treatment Plants.....	61
4.3.1. Closed-Loop Response of Linear Model	61
4.3.2. Closed-Loop Response of Nonlinear Model.....	64
4.4. Conclusions and Future Work	64
 5 AN EXCESS VOLUME MODEL TO DETERMINE CONVERSION IN AN EMULSION POLYMERIZATION REACTOR.....	66
5.1. Introduction.....	66
5.2. Motivation.....	67
5.3. One Parameter Excess Volume Model	69
5.3.1. Mathematical Formulation.....	69
5.3.2. Determining the Excess Volume Parameter.	70
5.3.3. Solving the One-Parameter Quadratic Equation.....	72
5.4. Redlich-Kister Two-Parameter Model.....	74
5.4.1. Mathematical Formulation.....	74
5.4.2. Determining the Excess Volume Parameters.....	75
5.4.3. Solving the Redlich-Kister Cubic Equation.....	75
5.5. Example – Polymerization of Styrene	76
5.5.1. Development of Models.....	76
5.5.2. Conversion Calculations.....	78
5.6. Copolymerization of Styrene and Butyl-Methacrylate	80
5.6.1. Development of Models.....	80
5.6.2. Conversion Calculations.....	81
5.7. Polymerization of Butyl-Methacrylate	81
5.7.1. Development of Models.....	81
5.7.2. Conversion Calculations.....	82
5.8. Conclusions.....	83

6 DESIGN AND CONTROL OF A CONTINUOUS SAMPLING AND DILUTION SYSTEM.....	85
6.1. Introduction.....	85
6.1.1. Motivation Behind the CSDS	85
6.1.2. Issues of CSDS Monitoring	86
6.1.3. Novelty of the CSDS	88
6.2. Design and Implementation of the CSDS.....	89
6.2.1. General Design.....	89
6.2.2. The Dynamic Model of the CSDS	91
6.2.3. Implementation	92
6.3. Automation and Control of the CSDS	94
6.4. Experimental and Simulated Responses of the CSDS.....	97
6.4.1. CSDS Open-Loop Response.....	97
6.4.2. CSDS Closed-Loop Response	97
6.4.3. CSDS Simulation.....	100
6.5. Conclusions and Future Work	102
7 CONCLUSIONS AND FUTURE WORK	104
7.1. Conclusions.....	104
7.2. Future Work	105
APPENDIX PROOF OF EQUATION (5.15)	106
LIST OF REFERENCES	108
BIOGRAPHICAL SKETCH	113

Abstract of Dissertation Presented to the Graduate School
of the University of Florida in Partial Fulfillment of the
Requirements for the Degree of Doctor of Philosophy

ANALYSIS OF ADVANCED CONTROL ALGORITHMS AND STUDIES ON
SENSOR TECHNOLOGIES FOR EMULSION POLYMERIZATION CONTROL

By

Brian Joseph Remark

May 2004

Chairman: Oscar D. Crisalle

Major Department: Chemical Engineering

The critical-direction theory is extended to include nonlinear elements through the introduction of the describing function and a general definition of the critical perturbation radius. The approach allows the calculation of the nonlinear Nyquist robust stability margin for systems with both structured and unstructured uncertainties, hence providing a conclusive test for robust stability. Finally, analytic expressions for finding the minimizing amplitude are obtained for circular uncertain value sets.

The robustness of predictive controllers is studied for systems with real parametric uncertainties that belong to an ellipsoidal or hyperbox domain. A parametric stability margin is proposed as a quantitative measure of robust stability as well as a robust controller design methodology that involves evaluating the parametric stability margin over a range of values for the predictive control tuning parameters. In addition, the standard predictive control algorithm is also modified to include a disturbance model to help improve regulatory performance. The resulting disturbance predictive control

demonstrated improved performance on linear systems. The performance on nonlinear cases is not satisfactory suggesting that further refinements, such as adaptive control schemes, may be necessary to handle such cases.

Two support tools for operating emulsion polymerization reactors are designed and implemented, namely a continuous sampling and dilution system and an online conversion estimator based on a densitometer. The dilution system is fully automated for data acquisition and real-time control. A dynamic first-principles model is developed and found to agree with experimental data. A new approach to estimate conversion on-line is developed through the use of a densitometer and the calculations are improved by the use of an excess-volume model. Both a one and two-parameter excess-volume models are analyzed, and examples are presented to illustrate the effectiveness of these models.

CHAPTER 1 INTRODUCTION

1.1 Motivation

Uncertainty is present in any physical system. This uncertainty directly translates to the model of the system used for control design, and is most often in the form of variations in model parameters. Control systems are required to be robust (*i.e.*, it functions satisfactorily under these uncertainties), and the design of these control schemes is known as robust control. One important aspect of the robust control problem is determining if a control system is robustly stable with respect to a given set of uncertainties.

Robust stability has been studied since the earliest days of feedback control. The earliest robust stability studies focused on frequency domain methods such as those based on Bode plots and Nyquist plots (Nyquist, 1932) which resulted in the gain and phase stability margins that are still used today. With the advent of the space race of the 1960's, the focus of control engineers was shifted away from frequency domain robust stability methods to the field of optimal control. The linear quadratic regulator (LQG) design, developed during this era, appeared to give controllers with good stability properties. However in the late 1970's it was found that LQGs lost their stability guarantees when uncertainty was present in the control system.

Due to this robust instability, H_∞ optimal control (Doyle, 1983; Doyle *et al.*, 1989; Francis and Zames, 1984; Safonov and Verma, 1985; Zames, 1981) was introduced to effectively deal with the robust stability and control issues. The theory considers

unstructured uncertainties where the only information known about the uncertainty is a norm bound. Normally more information is known about the uncertainty than a simple norm bound and other robust stability analysis methods have been developed that consider these structured uncertainties.

One robust stability analysis method for structure uncertainties is the critical-direction theory developed by Latchman and Crisalle (1995) and Baab *et al.* (2001) which addresses the problem of robust stability of systems affected by uncertainties that are characterized in terms of arbitrary frequency-domain value sets that can be convex or non-convex. The critical direction theory proposes the Nyquist robust stability margin as a measure of robust stability which is similar to other techniques that have been developed. The main advantage of this margin is that determining the Nyquist robust stability margin is a tractable problem as opposed to the challenging computations required previously.

Another type of structured uncertainty is real parametric uncertainty in the process model which began to receive renewed attention with the result of Kharitonov (1979) on the stability of interval polynomials. This result allows the stability analysis of a linear time invariant system to be performed as real uncertainty is added to the parameters (Bhattacharyya *et al.*, 1995). Consequently, the parametric stability margin is defined as the length of the smallest perturbation in the parameters which just destabilizes the closed loop system. The parametric stability margin is useful in controller design as a means of designing robustly stabilizing controllers.

Continuous emulsion polymerization reactors have several advantages over batch reactors; among them are (1) high reaction rates proving high yield, high molecular

weight polymers, (2) easier operation and control, and (3) more consistent polymer quality. However there are major problems associated with the operation of continuous reactors such as no true steady state, agglomeration, and fouling. The control of emulsion polymerization reactors requires advanced control strategies like those discussed earlier and would help remove or reduce these problems. However, subsystems must be developed that allow for the measurement of critical properties such as novel sensors to measure conversion and particle size distribution.

1.2 Objective and Structure of Dissertation

This dissertation is divided into two parts: theoretical process control and emulsion polymerization subsystems. Theoretical process control consists of three chapters including the nonlinear Nyquist robust stability margin, systematic algorithms for the design of robust predictive controllers, and the derivation of a disturbance predictive controller used in wastewater treatment plants. The emulsion polymerization subsystems include the determination of conversion on-line as well as the automation of a continuous sampling and dilution system that aids spectroscopic analysis.

The first goal of this dissertation is the extension of the critical direction theory to the more general case of nonlinear systems and is presented in Chapter 2. The key to extending the theory is the introduction of a generalized definition of the critical point in a fashion that preserves all previous results. Several nonlinear systems are analyzed and the minimizing amplitude discovered that maximizes the nonlinear Nyquist robust stability margin. The generalized critical direction theory is applied to nonlinear uncertain systems, and is used to calculate the required nonlinear Nyquist robust stability margin with high precision and in the context of a computationally manageable framework.

Chapter 3 proposes a systematic algorithm to design robust predictive controllers using the parametric stability margin. Hyperbox and ellipsoidal parametric uncertainties are considered and analyzed. Finally, examples are used to illustrate the design of the robust predictive controllers for both types of uncertainty.

The last section of theoretical process control is the development of a disturbance predictive controller for use in wastewater treatment plants and is discussed in Chapter 4. A brief introduction to the wastewater treatment plant model is given followed by the derivation of the disturbance predictive controller. The controller is connected to both a linear and nonlinear model of the wastewater treatment plant and compared to the predictive controller developed by Crisalle *et al.* (1989).

The final two chapters deal with subsystems required in the control of continuous emulsion polymerization reactors. Chapter 5 introduces an excess volume model to improve conversion estimates from densitometer data. The numerical issues associated with this model are discussed and three polymerization examples shown. Chapter 6 discusses the design and implementation of a continuous sampling and dilution system. The schematic and control scheme for the dilution system is shown and a dynamic model derived. Finally, the experimental and simulated closed loop systems are compared and future work described.

CHAPTER 2

COMPUTATION OF THE NONLINEAR NYQUIST ROBUST STABILITY MARGIN FOR UNCERTAIN SYSTEMS

2.1. Introduction

Much attention has been given to the problem of computing a robust stability margin for systems with frequency-domain uncertainty descriptions. The most notable contributions include the structured singular value μ (Doyle, 1982) and the multivariable stability margin k_m (Safonov, 1982). The *critical direction theory* developed by Latchman and Crisalle (1995) and by Latchman *et al.* (1997) introduced the *Nyquist robust stability margin* k_N , a scalar measure of robustness that has been effectively computed for single-input/single-output (SISO) systems with both convex (Latchman *et al.*, 1997) and non-convex (Baab *et al.*, 2001) uncertain value sets. However, all previous work has dealt with linear transfer functions. This chapter extends the critical direction theory to nonlinear systems, while preserving the key definitions and notation proposed for the linear theory.

2.2. Generalization of the Critical Direction Theory

2.2.1 Preliminaries

Consider the SISO linear time-invariant system

$$g(s) = g_o(s) + \delta(s) \tag{2.1}$$

where $g_o(s)$ is a known nominal transfer function and $\delta(s) \in \Delta$ is an unknown perturbation belonging to the unstructured uncertainty family Δ . Unstructured uncertainties have frequency-domain value sets that are circles with known radius $r(\omega)$,

namely, sets of the form $\Delta := \{\delta(s) : |\delta(j\omega)| \leq r(\omega) : r(\omega) > 0\}$. The uncertain system (2.1) is arranged in a negative feedback configuration featuring a nonlinear element $f(e)$, as shown in Figure 2.1. For simplicity in exposition, in Figure 2.1 we introduce a slight abuse in notation given that the map $f(e) : \Re \rightarrow \Re$ is a time-domain operator, while $g(s)$ is a Laplace-domain operator.

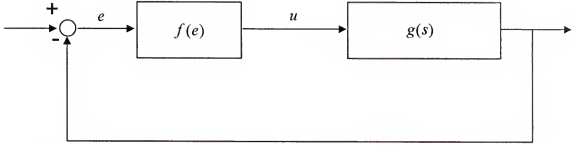


Figure 2.1. Closed-loop configuration of a nonlinear operator and an uncertain linear plant under negative feedback.

The robust stability analysis proposed involves three assumptions: (i) the nominal plant is stable under unity negative feedback, (ii) the nominal system $g_o(s)$ and the uncertain system $g(s)$ have the same number of unstable poles, and (iii) the higher harmonics of the nonlinear element $f(e)$ can be neglected.

2.2.2 Brief Review of the Critical Direction Theory

The critical direction theory was initially developed for linear systems, namely, for the special case of Figure 2.1 where $f(e) = 1$. Figure 2.2 shows a typical Nyquist diagram illustrating the nominal frequency response $g_o(j\omega)$. The figure also shows the point representing the nominal frequency response $g_o(j\omega)$ at a specific frequency ω_1 , along with its associated circular uncertainty value set $v(\omega_1)$ with radius $r(\omega)$. The critical perturbation radius $\rho_c(\omega_1)$ for the circular value-set is defined as the distance from the nominal point $g_o(j\omega_1)$ to the boundary of the uncertain circular value set, i.e.,

$$\rho_c(\omega) = |r(\omega)| \quad (2.2)$$

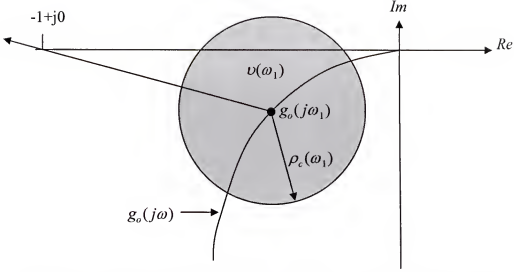


Figure 2.2. Critical direction theory illustrating a nominal point $g_o(j\omega)$ and its associated circular value set, $\nu(\omega_1)$, and critical perturbation radius $\rho_c(\omega_1)$.

The main result of the critical direction theory for linear systems is summarized in Theorem 2.1:

Let $g_o(j\omega)$ be a nominal SISO system with an associated circular uncertainty set Δ . Then the closed loop system given in Figure 1 with $f(e) = 1$ is robustly stable with respect to uncertainties $\delta(s) \in \Delta$ if and only if

$$\frac{\rho_c(\omega)}{|1 + g_o(j\omega)|} < 1 \quad \forall \omega$$

The proof is omitted for brevity. Details are given in Latchman (1997). The *Nyquist robust-stability margin* is then defined for SISO systems as

$$k_N(\omega) := \frac{\rho_c(\omega)}{|1 + g_o(j\omega)|} \quad (2.3)$$

Let $k_N := \max k_N(\omega)$. Then from Theorem 2.1 it is obvious that a necessary and sufficient condition for robust stability is given by the inequality

$$k_N < 1 \quad (2.4)$$

The calculation of the critical perturbation radius is often the most challenging problem to address when applying the critical direction theory to extract numerical values for the Nyquist robust stability margin (2.3); however, for the case of circular value sets, the task is extremely simple given the relationship (2.2).

2.2.3 Brief Review of the Describing Function Method

Consider now the nonlinear feedback loop shown in Figure 2.1 with $f(e) \neq 1$. The analysis of closed loop stability hinges on determining whether the limiting-stability condition of sustained signal oscillation can occur. In that limiting case, the input $e(t)$ to the nonlinear function $f(e)$ is sinusoidal, and it can be written as $e(t) = a \sin \omega t$ where $a > 0$ is the signal amplitude. Using a Fourier series expansion, the output from the nonlinear function can be written in the form

$$f(a \sin \omega t) = a'_0 + \sum_{k=1}^{\infty} (a'_k \cos k\omega t + b'_k \sin k\omega t)$$

which features a mean level a'_0 , a set of fundamental components of amplitudes a'_1 and b'_1 , and higher harmonic components of amplitudes a'_k and b'_k at frequencies $k\omega, k = 2, 3, \dots, \infty$ (Khalil, 1992).

The describing function method assumes that all the higher harmonics can be neglected, and as a consequence the nonlinear function $f(e)$ can then be approximated by its describing function $n(a)$, also referred to as the equivalent gain

$$n(a) = \frac{a_1 + jb_1}{a} \quad (2.5)$$

where

$$a_1(\omega) = \frac{1}{\pi} \int_0^{2\pi} f(x) \cos x dx$$

and

$$b_1(\omega) = \frac{1}{\pi} \int_0^{2\pi} f(x) \sin x dx$$

The describing function is a complex number that depends on the amplitude of the sinusoid, and it can be displayed as a locus on the complex plane.

The validity of this method relies on the assumption that the higher harmonics produced by the nonlinear function $f(e)$ can be discarded (Leigh, 1983). This is ensured in all cases where the transfer function $g(s)$ behaves as a low-pass filter.

2.3. Critical Direction Theory for Nonlinear Systems

In this section the SISO critical direction theory is extended to nonlinear systems. The concepts of critical direction, critical perturbation radius, and critical point are appropriately redefined to take into account the nonlinearity of the system.

After approximating the nonlinear element $f(e)$ by its describing function $n(a)$, the characteristic equation for the control configuration in Figure 2.1 is of the form

$$1 + n(a)g(s) = 0$$

Rearranging terms

$$g(s) = -\frac{1}{n(a)} \quad (2.6)$$

In the suite, we refer to the Nyquist map of $-1/n(a)$ for all $a > 0$ as the *critical loci*. The robust stability of the closed loop is ensured if the value sets of $g(j\omega)$ exclude all points belonging to the critical loci. Under the assumptions established earlier, the *critical loci exclusion principle* is in fact a necessary and sufficient condition for robust

closed loop stability. The following definitions introduce concepts illustrated in Figure 2.3 and Figure 2.4 that are useful for formulating a nonlinear critical direction theory for systems with a convex and non-convex uncertainty description respectively.

1. The critical directions

$$d_c(j\omega, a) = - \frac{g_o(j\omega) + \frac{1}{n(a)}}{\left| g_o(j\omega) + \frac{1}{n(a)} \right|} = - \frac{1 + g_o(j\omega)n(a)}{|1 + g_o(j\omega)n(a)|} \frac{|n(a)|}{n(a)}$$

are interpreted as a set of unit vectors originating at $g_o(j\omega)$ and pointing towards the critical loci.

2. The critical cone $\theta_c(\omega)$ maps all critical directions from the nominal point to the critical loci.

3. The critical template $v_c(\omega)$ contains the uncertainty defined by the intersection of the critical cone and uncertainty value set.

4. The critical perturbation radii for convex systems is defined as

$$\rho_c(\omega, a) = \max_{\alpha \in \mathbb{R}_+} \left\{ \alpha \mid z = g_o(j\omega) + \alpha d_c(\omega, a) \in v_c(\omega) \right\} \quad (2.7)$$

Equation (2.7) states that the critical perturbation radius for a convex critical value set $v_c(\omega)$ is the distance from the nominal point $g_o(\omega)$ to the uncertain value set boundary $\partial v(\omega)$ along the critical direction. Equation (2.7), however, is not suitable for non-convex critical value sets $v_c(\omega)$. A general definition of the critical perturbation radius similar to Baab *et al.* (2001) is proposed which is applicable to both the convex and non-convex cases

$$\rho_c(\omega, a) := \begin{cases} \left| \frac{1}{n(a)} + g_o(j\omega) \right| - \xi(\omega) & \text{if } -\frac{1}{n(a)} \notin v(\omega) \\ \left| \frac{1}{n(a)} + g_o(j\omega) \right| + \xi(\omega) & \text{otherwise} \end{cases} \quad (2.8)$$

where

$$\xi(\omega) = \min_{z \in \beta_c(\omega)} \left| \frac{1}{n(a)} + z \right| \quad (2.9)$$

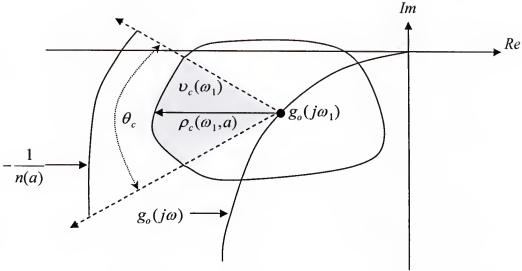


Figure 2.3. A convex value set with critical cone, critical perturbation radius, and critical value set illustrated).

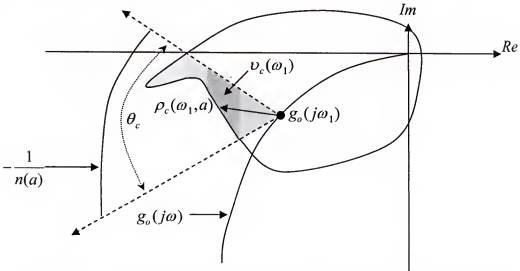


Figure 2.4. A non-convex value set with critical cone, critical perturbation radius, and critical value set illustrated.

Equation (2.8) represents the distance from the critical loci to the point in $\beta_c(\omega)$ that is closest to the critical loci. The upper statement in equation (2.8) states that when the critical loci is not an element of the uncertainty value set $\nu(\omega)$, the critical perturbation radius $\rho_c(\omega)$ is defined as the difference between the two distances, namely, the distance from the critical loci to the nominal point (represented by $\left| \frac{1}{n(a)} + g_o(j\omega) \right|$) and the distance from the critical loci to the closest critical-boundary intersection (represented by $\xi(\omega)$). Conversely, when the critical loci is an element of the uncertainty value set, the lower statement in equation (2.8) states that the critical perturbation is the sum of the two respective distances. When the critical value set is convex, equation (2.8) reduces to equation (2.7) because there is only one critical boundary intersection. To calculate the critical perturbation radius from (2.8), it is necessary to have full knowledge of the critical boundary intersections $\beta_c(\omega)$ and to evaluate whether the set membership condition $-1/n(a) \in \nu(\omega)$ holds. For either definition, it should be noted that $\rho_c(\omega) \geq 0$ for all frequencies and is a function of frequency and of the amplitude to the describing function.

At a given frequency ω_1 , the *critical-line* set is defined as the set of oriented lines with origin at the nominal point $g_o(j\omega_1)$, and that pass through any point in the critical loci $-1/n(a)$. The critical perturbation radius $\rho_c(\omega_1, a)$ is interpreted as the distance from the nominal point to the point where the critical line defined for an amplitude a intersects with the uncertain value set. Finally, the Nyquist robust stability margin for nonlinear systems is defined as

$$k_N(\omega) := \max_{a>0} \frac{\rho_c(\omega, a)}{\left| \frac{1}{n(a)} + g_o(j\omega) \right|} \quad (2.10)$$

or equivalently,

$$k_N(\omega) = \max_{a>0} \frac{|n(a)|\rho_c(\omega, a)}{|g_o(j\omega) + n(a)|} \quad (2.11)$$

The following robust-stability theorems for nonlinear systems use the same assumptions invoked previously with Theorem 2.2 illustrated below.

Let $g_o(s)$ be a nominal system with associated circular uncertainty set Δ . Then the closed loop system given in Figure 1 is robustly stable with respect to all uncertainties $\delta(s) \in \Delta$ if and only if

$$k_N(\omega) < 1 \quad (2.12)$$

for all frequencies $\omega > 0$.

Proof. A complete proof is given in Latchman and Crisalle (1997) for the case where $\nu_c(\omega)$ is convex. For non-convex systems, the general definition (2.8) of $\rho_c(\omega)$ is exploited. From the critical loci exclusion principle the uncertain closed loop is stable if and only if $-1/n(a) \notin \nu(\omega) \quad \forall \omega$. Therefore, to prove that (2.12) is sufficient for robust stability, it must be shown that if $k_N(\omega) < 1 \quad \forall \omega$ then $-1/n(a) \notin \nu(\omega) \quad \forall \omega$. To prove this by contradiction, first assume that $k_N(\omega) < 1 \quad \forall \omega$ and that $\exists \omega$ such that $-1/n(a) \in \nu(\omega)$. Apply definitions (2.8) and (2.10) for a frequency at which $-1/n(a) \in \nu(\omega)$ to yield

$$k_N(\omega) = \frac{\rho_c(\omega)}{\left| \frac{1}{n(a)} + g_o(j\omega) \right|} = \frac{\left| \frac{1}{n(a)} + g_o(j\omega) \right| + \xi(\omega)}{\left| \frac{1}{n(a)} + g_o(j\omega) \right|} = 1 + \frac{\xi(\omega)}{\left| \frac{1}{n(a)} + g_o(j\omega) \right|}$$

where $\xi(\omega)$ is a non-negative real scalar given by (2.9). Therefore $k_N(\omega) \geq 1$ for at least one frequency which contradicts the assumption. Thus, if $k_N(\omega) < 1 \quad \forall \omega$ then it must follow that $-1/n(a) \notin \nu(\omega) \quad \forall \omega$. To prove that (2.12) is necessary for robust stability, it must be shown that if $-1/n(a) \notin \nu(\omega) \quad \forall \omega$ then $k_N(\omega) < 1 \quad \forall \omega$. Apply definitions (2.8) and (2.10) if $-1/n(a) \notin \nu(\omega)$ to yield

$$k_N(\omega) = \frac{\rho_c(\omega)}{\left| \frac{1}{n(a)} + g_o(j\omega) \right|} = \frac{\left| \frac{1}{n(a)} + g_o(j\omega) \right| - \xi(\omega)}{\left| \frac{1}{n(a)} + g_o(j\omega) \right|} = 1 - \frac{\xi(\omega)}{\left| \frac{1}{n(a)} + g_o(j\omega) \right|} \quad \forall \omega$$

where $\xi(\omega)$ is given by (2.9). Because we assumed that $-1/n(a) \notin \nu(\omega)$ it follows that $-1/n(a) \notin \beta_c(\omega)$ and thus $\xi(\omega)$ must be a positive number. This fact is used in the above equation to lead to the conclusion that $k_N(\omega) < 1 \quad \forall \omega$ and that equation (2.12) is a necessary and sufficient condition for robust stability.

It should be noted that the Nyquist robust stability margin must be less than 1 at all frequencies and amplitudes to guarantee stability; therefore, $k_N(\omega, a)$ must be maximized over all frequencies and amplitudes in order to assess the robust stability. Let

$$k_N := \max_{\omega \geq 0} k_N(\omega) \quad (2.13)$$

Then, from Theorem 2.2 it follows that a necessary and sufficient condition for the robust stability of the uncertain nonlinear closed loop is that $k_N < 1$.

Theorem 2.2 states that the scalar $k_N(\omega)$ is used to characterize the robust stability of the closed-loop system. The computation of $k_N(\omega)$ requires the knowledge of the critical perturbation radius defined in (2.8). The challenging task in this problem is to calculate the critical perturbation radius.

When $v_c(\omega)$ is convex, equation (2.7) indicates that $\rho_c(\omega)$ is the distance from the nominal point $g_o(j\omega)$ and the unique point where the critical line intersects the boundary of the uncertain value set $v(\omega)$. However, when $v_c(\omega)$ is non-convex there are multiple points where the critical line intersects $v(\omega)$. Then equation (2.8) states that $\rho_c(\omega)$ is a function of the distance between $g_o(j\omega)$ and the boundary-intersection point that is closest to the critical loci. Because the convexity of $v_c(\omega)$ may not be known *a priori*, the general definition of the critical perturbation radius (2.8) allows the critical direction theory to be applied to a more general class of uncertain systems, especially the case of real affine uncertain systems.

2.4. Special Cases Under Consideration

2.4.1 Derivations Using Circular Value Sets

For the circular value sets considered, the critical radius $\rho_c(\omega, a)$ required in (2.10) or (2.11) for the calculation of $k_N(\omega, a)$ is explicitly given by (2.2), namely $\rho_c(\omega, a) = r(\omega)$ is a constant at each frequency and is independent of the amplitude a . Consequently, the optimization (2.10) or (2.11) required to determine the Nyquist robust stability margin can be carried out in an efficient fashion by minimizing the distance

$$d(\omega, a^*) = \left| \frac{1}{n(a^*)} + g_o(j\omega) \right| \quad (2.14)$$

from the nominal point to the critical loci. Define now the *minimizing amplitude*

$$a^*(\omega) = \arg \min_{a>0} \left| \frac{1}{n(a)} + g_o(j\omega) \right|$$

A value for $k_N(\omega)$ can then be obtained from (2.10) or (2.11) at each frequency if $a^*(\omega)$ is known. Theorem 2.3 illustrated below provides details of the procedure.

Let a circular uncertain value set described by a radius $r(\omega)$ and let $d(\omega, a^)$ denote the minimum distance. Then the Nyquist robust stability margin is given by*

$$k_N(\omega) = \frac{r(\omega)}{d(\omega, a^*)} \quad (2.15)$$

where the minimizing amplitude is given by

$$a^* = \min \{d(\omega, a_1^*), d(\omega, a_2^*), \dots, d(\omega, a_k^*)\}$$

and where the set $\{a_1^*, a_2^*, \dots, a_k^*\}$ represents all roots of the equation

$$\frac{\alpha + \beta}{(n_r(a)^2 + n_i(a)^2)^2} = 0 \quad (2.16)$$

where

$$\alpha(\omega, a) = (-n_r(a)^2 g_{or}(j\omega) + 2n_r(a)n_i(a)g_{oi}(j\omega) + n_i(a)^2 g_{or}(j\omega) - n_r(a)) \frac{dn_r(a)}{da} \quad (2.17)$$

$$\beta(\omega, a) = (n_i(a)^2 g_{oi}(j\omega) - 2n_r(a)n_i(a)g_{or}(j\omega) - n_r(a)^2 g_{oi}(j\omega) - n_i(a)) \frac{dn_i(a)}{da} \quad (2.18)$$

Proof. The derivative of (2.14) must be calculated to find the minimizing amplitude $a^*(\omega)$. First, rewrite equation (2.14) as

$$d(\omega, a) = \left\{ \frac{1}{n(a)n(a)} + \frac{\overline{g_o(j\omega)}}{n(a)} + \frac{g_o(j\omega)}{n(a)} + g_o(j\omega)\overline{g_o(j\omega)} \right\}^{1/2} \quad (2.19)$$

The derivatives of each term inside the braces in (2.19) are determined as follows. Split the nominal point and describing function into their respective real and imaginary parts, *i.e.*,

$$g_o(j\omega) = g_{or}(j\omega) + jg_{oi}(j\omega)$$

$$\overline{g_o(j\omega)} = g_{or}(j\omega) - jg_{oi}(j\omega)$$

and

$$n(a) = n_r(a) + jn_i(a)$$

$$\overline{n(a)} = n_r(a) - jn_i(a)$$

Now, the derivative of $\frac{1}{n(a)\overline{n(a)}}$ can be written as

$$\frac{d}{da} \left(\frac{1}{|n(a)|^2} \right) = \frac{-2 \left(n_r(a) \frac{dn_r(a)}{da} + n_i(a) \frac{dn_i(a)}{da} \right)}{(n_r(a)^2 + n_i(a)^2)^2} \quad (2.20)$$

The terms $\frac{g_o(j\omega)}{n(a)} + \frac{\overline{g_o(j\omega)}}{\overline{n(a)}}$ in equation (2.19) are rearranged and simplified to yield

$$\frac{g_o(j\omega)}{n(a)} + \frac{\overline{g_o(j\omega)}}{\overline{n(a)}} = \frac{2(n_r(a)g_{or}(j\omega) - n_i(a)g_{oi}(j\omega))}{n_r(a)^2 + n_i(a)^2} \quad (2.21)$$

Using the quotient rule, the derivative of (2.21) with respect to the amplitude can be written as

$$\begin{aligned} \frac{d}{da} \left(\frac{g_o(j\omega)}{n(a)} + \frac{\overline{g_o(j\omega)}}{\overline{n(a)}} \right) &= \frac{2 \left(g_{or}(j\omega) \frac{dn_r(a)}{da} - g_{oi}(j\omega) \frac{dn_i(a)}{da} \right)}{(n_r(a)^2 + n_i(a)^2)} \\ &- \frac{4(n_r(a)g_{or}(j\omega) - n_i(a)g_{oi}(j\omega)) \left(n_r(a) \frac{dn_r(a)}{da} + n_i(a) \frac{dn_i(a)}{da} \right)}{(n_r(a)^2 + n_i(a)^2)^2} \end{aligned} \quad (2.22)$$

Finally, the term $g_o(j\omega)\overline{g_o(j\omega)}$ is not dependent upon the amplitude a , making its derivative identically zero. The derivative of (2.19) is readily obtained using equations (2.20) and (2.22) and carrying out straightforward algebraic manipulations, resulting in

$$\frac{d}{da}(d(\omega, a)) = \frac{1}{d(\omega, a)^{1/2}} \frac{\alpha + \beta}{(n_r(a)^2 + n_i(a)^2)^2} \quad (2.23)$$

where α and β are respectively given by (2.17) and (2.18). Setting (2.23) equal to zero and recognizing that $d(\omega, a) \neq 0$ by the assumption of nominal stability yields equation (2.16).

The robustness analysis for non-circular templates is challenging because both the critical perturbation radius and the distance from the nominal point to the critical loci change as a function of frequency and amplitude. To simplify the calculation, it is common to circumscribe an arbitrary shaped template with an appropriate circle (Bhattacharya, 1993), making the uncertainty value set $\nu(\omega)$ become a circle with radius $r(\omega)$. Therefore at each frequency, the critical perturbation radius becomes a constant equal to the radius of the circle and independent of the amplitude. The analysis then proceeds as in the circular case. The resulting condition $k_N < 1$ is now sufficient only, given that the original value set has been substituted for a .

Theorem 2.3 can be used to derive analytical expressions for the amplitude $a^*(\omega)$ that solve the equation $d(d(\omega, a))/da = 0$ for several nonlinear operators of interest. Table 2.1 shows four nonlinear maps reported by Mohler (1991), which afford analytical treatment. The first column of Table 2.1 shows in graphical form the nonlinear operator considered. The parameter m represents the point where the map $f(e)$ intercepts the

ordinate, a is the magnitude of the map when it intercepts the positive abscissa, and k represents the slope of the map. The next two columns show the real and imaginary parts for describing function of the map, and finally the last column gives an analytical expression for the candidate amplitudes that must be considered as possible minimizers of (2.14). For example, the third row shows that there are two amplitudes that set the derivative (2.16) equal to zero, namely $a_1^*(\omega) = \frac{-4m}{\pi} \frac{g_{or}(\omega)}{1 + kg_{or}(\omega)}$ and $a_2^*(\omega) \rightarrow \infty$. Hence, the minimizer is to be selected from these two candidate amplitudes.

The nonlinear operator for saturation is shown below. This nonlinear element can be approximated by the following describing function

$$\begin{aligned} n(a) &= k \quad \text{for } \frac{a}{d} \leq 1 \\ n(a) &= kNu \quad \text{else} \end{aligned} \quad (2.24)$$

where

$$Nu = \frac{2}{\pi} \left[\sin^{-1} \left(\frac{d}{a} \right) + \frac{d}{a} \left(1 - \frac{d^2}{a^2} \right)^{1/2} \right]$$

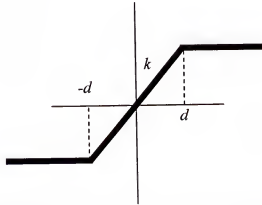
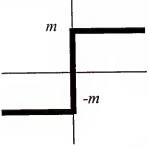
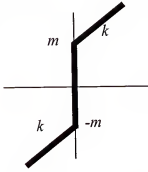
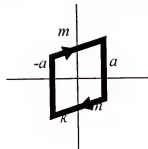


Figure 2.5. Graph for saturation illustrating the slope k and endpoints d .

Table 2.1. Describing functions and analytical expressions for the amplitudes that solve the equation $d(d(\omega, a))/da = 0$.

$f(e)$	$n_r(a)$	$n_i(a)$	Candidate minimizing amplitudes
	$\frac{4m}{\pi a}$	0	$a_1^*(\omega) = \frac{-4mg_{or}(\omega)}{\pi}$
	$k + \frac{4m}{\pi a}$	0	$a_1^*(\omega) = \frac{-4m}{\pi} \frac{g_{or}(\omega)}{1 + kg_{or}(\omega)}, \quad a_2^*(\omega) = \infty$
	k	$\frac{4m}{\pi a}$	$a_1^*(\omega) = \frac{8mg_{oi}(\omega)}{\pi\theta_1(\omega)}, \quad a_2^*(\omega) = \frac{8mg_{oi}(\omega)}{\pi\theta_2(\omega)},$ $a_3^*(\omega) = \infty$ $\theta_1(\omega) = 2kg_{or}(\omega) + 1 - \sqrt{4k^2(g_{or}^2(\omega) + g_{oi}^2(\omega)) + 4kg_{or}(\omega) + 1}$ $\theta_2(\omega) = 2kg_{or}(\omega) + 1 + \sqrt{4k^2(g_{or}^2(\omega) + g_{oi}^2(\omega)) + 4kg_{or}(\omega) + 1}$

The approach used earlier cannot yield a simple analytic expression because of the complex nature of the describing function. However, an analytical expression can be

obtained analyzing the describing function. The analytic expressions for the minimum distance from the nominal point to the critical loci are given as follows

$$\begin{aligned} d_1^*(\omega) &= \left(g_{oi}^2(\omega) + g_{or}^2(\omega) + \frac{2\pi g_{or}(\omega)}{2.3768k} + \left(\frac{\pi}{2.3768k} \right)^2 \right)^{1/2} \\ d_2^*(\omega) &= |g_{oi}(\omega)| \\ d_3^*(\omega) &= |g_o(\omega)| \end{aligned} \quad (2.25)$$

Hence, the minimizing distance $d^*(\omega)$ is to be taken from one of the three candidate distances.

Proof. The describing function given by (2.24) maps to a straight line segment on the Nyquist plane as shown in Figure 2.6.



Figure 2.6. Nyquist map of the saturation describing function. Note that the endpoint depends only on the slope of the saturation line.

There are now three regions where the nominal point $g_o(\omega)$ may lie: (1) to the left of the line segment, (2) above or below the line segment, or (3) to the right of the line segment and we will treat each case in turn. If $g_o(\omega)$ lies to the left of the line segment, then the shortest distance will be from $g_o(\omega)$ to the endpoint $-\frac{\pi}{2.3768k}$ which is given by

$$d_1^2(\omega) = |g_{oi}(\omega)|^2 + \left(g_{or}(\omega) + \frac{\pi}{2.3768k} \right)^2$$

which can be simplified to yield $d_1^*(\omega)$. When the nominal point lies directly above or below the line segment, region (2), the shortest distance will simply be the magnitude of the imaginary part of the nominal point $g_{oi}(\omega)$. The last area to analyze is when $g_o(\omega)$

lies to the right of the line segment. The shortest distance will then be the distance from the origin to the nominal point $g_o(\omega)$. Thus the minimizing distance is given by the magnitude of the nominal point illustrated by $d_3^*(\omega)$.

2.4.2 Real Affine Parametric Uncertainty

The generalized critical direction theory developed in Section 2.3 is specialized to systems with real affine parametric uncertainties of the form

$$g(s, \mathbf{q}) = \frac{n_0(s) + \sum_{i=1}^p q_i n_i(s)}{d_0(s) + \sum_{i=1}^p q_i d_i(s)}, \quad \mathbf{q} \in \mathcal{Q} \quad (2.26)$$

where

$$n_0(s) := \sum_{k=0}^{\ell} n_{0k} s^k$$

and

$$d_0(s) := \sum_{k=0}^m d_{0k} s^k$$

are known nominal polynomials,

$$n_i(s) = \sum_{k=0}^{\ell} n_{ik} s^k$$

and

$$d_i(s) = \sum_{k=0}^m d_{ik} s^k$$

are known perturbation polynomials, and $\mathbf{q} = [q_1 \ q_2 \ \dots \ q_p]^T \in R^p$ is a vector of real perturbation parameters belonging to the bounded rectangular polytope

$$\mathcal{Q} = \left\{ \mathbf{q} \in \mathbb{R}^p \mid q_i^- \leq q_i \leq q_i^+, i = 1, 2, \dots, p \right\} \quad (2.27)$$

where q_i^- and q_i^+ , $i = 1, 2, \dots, p$ are finite real bounds. Equations (2.26) and (2.27) define a class of finite dimensional, linear, time-invariant, real plants with affine uncertainties.

The first step in determining the generalized critical perturbation radius for the uncertain system (2.26) - (2.27) is to determine whether the critical loci $-1/n(a)$ belongs to the uncertainty set $\nu(\omega)$.

The affine uncertain system (2.26) can be written in vector-matrix form

$$g(s, \mathbf{q}) = \frac{\begin{bmatrix} 1 & s & \dots & s^{\ell-1} & s^\ell \end{bmatrix} \left(\begin{bmatrix} n_{00} \\ n_{01} \\ \vdots \\ n_{0\ell} \end{bmatrix} + \begin{bmatrix} n_{10} & n_{20} & \dots & n_{p0} \\ n_{11} & n_{21} & \dots & n_{p1} \\ \vdots & \vdots & \ddots & \vdots \\ n_{1\ell} & n_{2\ell} & \dots & n_{p\ell} \end{bmatrix} \begin{bmatrix} q_1 \\ q_2 \\ \vdots \\ q_p \end{bmatrix} \right)}{\begin{bmatrix} 1 & s & \dots & s^{m-1} & s^m \end{bmatrix} \left(\begin{bmatrix} d_{00} \\ d_{01} \\ \vdots \\ d_{0m} \end{bmatrix} + \begin{bmatrix} d_{10} & d_{20} & \dots & d_{p0} \\ d_{11} & d_{21} & \dots & d_{p1} \\ \vdots & \vdots & \ddots & \vdots \\ d_{1m} & d_{2m} & \dots & d_{pm} \end{bmatrix} \begin{bmatrix} q_1 \\ q_2 \\ \vdots \\ q_p \end{bmatrix} \right)} \quad (2.28)$$

$$= \frac{\mathbf{s}_n^T (\mathbf{n}_0 + \mathbf{N}_p \mathbf{q})}{\mathbf{s}_d^T (\mathbf{d}_0 + \mathbf{D}_p \mathbf{q})}$$

where \mathbf{s}_n and \mathbf{s}_d are vectors of lengths $\ell + 1$ and $m + 1$, containing powers of the Laplace variable s , and where $\mathbf{n}_0 \in \mathbb{R}^{\ell+1}$, $\mathbf{d}_0 \in \mathbb{R}^{m+1}$, $\mathbf{N}_p \in \mathbb{R}^{(\ell+1) \times p}$ and $\mathbf{D}_p \in \mathbb{R}^{(m+1) \times p}$ are constant vectors and matrices that represent the structure of the affine parametric uncertainty. The value set (2.28) is evaluated at a frequency ω by substituting $s = j\omega$ to yield

$$g(j\omega, \mathbf{q}) = \frac{\mathbf{s}_{n,R}^T (\mathbf{n}_{0,R} + \mathbf{N}_{p,R} \mathbf{q}) + j \mathbf{s}_{n,I}^T (\mathbf{n}_{0,I} + \mathbf{N}_{p,I} \mathbf{q})}{\mathbf{s}_{d,R}^T (\mathbf{d}_{0,R} + \mathbf{D}_{p,R} \mathbf{q}) + j \mathbf{s}_{d,I}^T (\mathbf{d}_{0,I} + \mathbf{D}_{p,I} \mathbf{q})}, \mathbf{q} \in \mathcal{Q} \quad (2.29)$$

where

$$\mathbf{s}_{n,R}^T = [1 \quad -\omega^2 \quad \omega^4 \quad -\omega^6 \quad \dots] \in \mathbb{R}^{\lceil \ell/2 \rceil + 1}, \mathbf{s}_{n,I}^T = [\omega \quad -\omega^3 \quad \omega^5 \quad -\omega^7 \quad \dots] \in \mathbb{R}^{\lceil (\ell+1)/2 \rceil}$$

$$\mathbf{s}_{d,R}^T = [1 \quad -\omega^2 \quad \omega^4 \quad -\omega^6 \quad \dots] \in \mathbb{R}^{\lceil m/2 \rceil + 1}, \mathbf{s}_{d,I}^T = [\omega \quad -\omega^3 \quad \omega^5 \quad -\omega^7 \quad \dots] \in \mathbb{R}^{\lceil (m+1)/2 \rceil}$$

$$\mathbf{n}_{0,R} = \begin{bmatrix} n_{00} \\ n_{02} \\ \vdots \end{bmatrix} \in \mathbb{R}^{\lceil \ell/2 \rceil + 1}, \quad \mathbf{N}_{p,R} = \begin{bmatrix} n_{10} & n_{20} & \dots & n_{p0} \\ n_{12} & n_{22} & \dots & n_{p2} \\ \vdots & \vdots & \dots & \vdots \end{bmatrix} \in \mathbb{R}^{(\lceil \ell/2 \rceil + 1) \times p}$$

$$\mathbf{n}_{0,I} = \begin{bmatrix} n_{01} \\ n_{03} \\ \vdots \end{bmatrix} \in \mathbb{R}^{\lceil (\ell+1)/2 \rceil}, \quad \mathbf{N}_{p,I} = \begin{bmatrix} n_{11} & n_{21} & \dots & n_{p1} \\ n_{13} & n_{23} & \dots & n_{p3} \\ \vdots & \vdots & \dots & \vdots \end{bmatrix} \in \mathbb{R}^{\lceil (\ell+1)/2 \rceil \times p}$$

$$\mathbf{d}_{0,R} = \begin{bmatrix} d_{00} \\ d_{02} \\ \vdots \end{bmatrix} \in \mathbb{R}^{\lceil m/2 \rceil + 1}, \quad \mathbf{D}_{p,R} = \begin{bmatrix} d_{10} & d_{20} & \dots & d_{p0} \\ d_{12} & d_{22} & \dots & d_{p2} \\ \vdots & \vdots & \dots & \vdots \end{bmatrix} \in \mathbb{R}^{(\lceil m/2 \rceil + 1) \times p}$$

and

$$\mathbf{d}_{0,I} = \begin{bmatrix} d_{01} \\ d_{03} \\ \vdots \end{bmatrix} \in \mathbb{R}^{\lceil (m+1)/2 \rceil}, \quad \mathbf{D}_{p,I} = \begin{bmatrix} d_{11} & d_{21} & \dots & d_{p1} \\ d_{13} & d_{23} & \dots & d_{p3} \\ \vdots & \vdots & \dots & \vdots \end{bmatrix} \in \mathbb{R}^{\lceil (m+1)/2 \rceil \times p}$$

where $\lceil \bullet \rceil$ represents the greatest integer function.

Now consider a point on the critical loci $w = w_R + jw_I \in -1/n(a)$. It can be shown that $w \in \nu(\omega)$ if and only if there exists a vector $\mathbf{q} \in \mathcal{Q}$ such that $g(j\omega, \mathbf{q}) = w$. Using (2.29) this requirement is equal to obtaining a vector $\mathbf{q} \in \mathcal{Q}$ that solves the equation

$$\frac{\mathbf{s}_{n,R}^T(\mathbf{n}_{0,R} + \mathbf{N}_{p,R}\mathbf{q}) + j\mathbf{s}_{n,I}^T(\mathbf{n}_{0,I} + \mathbf{N}_{p,I}\mathbf{q})}{\mathbf{s}_{d,R}^T(\mathbf{d}_{0,R} + \mathbf{D}_{p,R}\mathbf{q}) + j\mathbf{s}_{d,I}^T(\mathbf{d}_{0,I} + \mathbf{D}_{p,I}\mathbf{q})} = w_R + j w_I \quad (2.30)$$

This can be characterized by a linear equality problem shown by Theorem 2.4:

Let $w \in -1/n(a)$ point with finite magnitude on the critical loci. Then

$w \in \nu(\omega)$ if and only if there exists a feasible solution $\mathbf{q} \in \mathbb{R}^p$ to the linear equality

$$\mathbf{A}(w) \mathbf{q} = \mathbf{b}(w) \quad (2.31)$$

subject to the linear-inequality constraint

$$\begin{bmatrix} 1 & 0 & 0 & \cdots & 0 \\ -1 & 0 & 0 & \cdots & 0 \\ 0 & 1 & 0 & \cdots & 0 \\ 0 & -1 & 0 & \cdots & 0 \\ \vdots & \vdots & \vdots & \ddots & \vdots \\ 0 & 0 & 0 & \cdots & 1 \\ 0 & 0 & 0 & \cdots & -1 \end{bmatrix} \mathbf{q} \leq \begin{bmatrix} q_1^+ \\ -q_1^- \\ q_2^+ \\ -q_2^- \\ \vdots \\ q_p^+ \\ -q_p^- \end{bmatrix} \quad (2.32)$$

where

$$\mathbf{A}(w) := \begin{bmatrix} \mathbf{s}_{n,R}^T \mathbf{N}_{p,R} - w_R \mathbf{s}_{d,R}^T \mathbf{D}_{p,R} + w_I \mathbf{s}_{d,I}^T \mathbf{D}_{p,I} \\ \mathbf{s}_{n,I}^T \mathbf{N}_{p,I} - w_R \mathbf{s}_{d,I}^T \mathbf{D}_{p,I} - w_I \mathbf{s}_{d,R}^T \mathbf{D}_{p,R} \end{bmatrix} \in \mathbb{R}^{2 \times p} \quad (2.33)$$

$$\mathbf{b}(w) := \begin{bmatrix} -\mathbf{s}_{n,R}^T \mathbf{n}_{0,R} + w_R \mathbf{s}_{d,R}^T \mathbf{d}_{0,R} - w_I \mathbf{s}_{d,I}^T \mathbf{d}_{0,I} \\ -\mathbf{s}_{n,I}^T \mathbf{n}_{0,I} + w_R \mathbf{s}_{d,I}^T \mathbf{d}_{0,I} + w_I \mathbf{s}_{d,R}^T \mathbf{d}_{0,R} \end{bmatrix} \in \mathbb{R}^2 \quad (2.34)$$

Proof. A finite point $w \in -1/n(a)$ belongs to $\nu(\omega)$ if and only if there exists a vector $\mathbf{q} \in Q$ that satisfies equation (2.30). Since the denominator of the left hand side of (2.30) is non-zero because of the finite magnitude of w , the equality can be rearranged and the real and imaginary parts separated to yield

$$\begin{bmatrix} \mathbf{s}_{n,R}^T \mathbf{N}_{p,R} - w_R \mathbf{s}_{d,R}^T \mathbf{D}_{p,R} + w_I \mathbf{s}_{d,I}^T \mathbf{D}_{p,I} \\ \mathbf{s}_{n,I}^T \mathbf{N}_{p,I} - w_R \mathbf{s}_{d,I}^T \mathbf{D}_{p,I} - w_I \mathbf{s}_{d,R}^T \mathbf{D}_{p,R} \end{bmatrix} \mathbf{q} = \begin{bmatrix} -\mathbf{s}_{n,R}^T \mathbf{n}_{0,R} + w_R \mathbf{s}_{d,R}^T \mathbf{d}_{0,R} - w_I \mathbf{s}_{d,I}^T \mathbf{d}_{0,I} \\ -\mathbf{s}_{n,I}^T \mathbf{n}_{0,I} + w_R \mathbf{s}_{d,I}^T \mathbf{d}_{0,I} + w_I \mathbf{s}_{d,R}^T \mathbf{d}_{0,R} \end{bmatrix}$$

which is equal to (2.31) after the definitions given in (2.33) and (2.34) are substituted. From the definition of Q in (2.27), the constraint that $\mathbf{q} \in Q$ can be described by the linear inequality (2.32). Therefore, $w \in -1/n(a)$ is an element of $v(\omega)$ if and only if there exists a feasible solution to the linear program defined by equations (2.31) and (2.32).

The computation of the Nyquist robust stability margin $k_N(\omega)$ for affine systems (2.26) requires that the critical perturbation radius $\rho_c(\omega)$ be calculated first. As illustrated by (2.8) and (2.9), this requires determining the set $\beta_c(\omega)$. Once all the elements of $\beta_c(\omega)$ have been determined, it is straightforward to calculate $\rho_c(\omega)$ from formulas. For the case of affine-uncertain systems of the form given by (2.26), Baab *et al.* (2001) have identified a two-step strategy that effectively determines the critical boundary-intersections set $\beta_c(\omega)$. For brevity it has been omitted here.

2.5. Examples

2.5.1 Circular Value Set with Simple Describing Function

Consider the open-loop unstable system

$$g_o(s) = \frac{1}{-s + 10}$$

with an associated unstructured (circular) uncertainty with radius

$$r(\omega) = \left| \frac{1}{-j\omega + 10} \right|$$

and a nonlinear operator $f(e)$ of the form given in the last row of Table 2.1 with $k = 2$ and $m = 1$. The describing function in this case is

$$n(a) = 2 + \frac{4}{\pi a} j$$

It is straightforward to show that the nominal closed-loop system (*i.e.*, when $r(\omega) = 0 \forall \omega$) is stable.

Figure 2.7 shows the nominal point $g_o(j\omega)$ at a frequency $\omega = 10$, along with a circular disk representing the uncertain value set at this frequency. At this frequency, $\rho_c(\omega, a) = r(\omega) = 0.0707$. The figure also shows the critical loci for amplitudes ranging from 0.0001 to 0.5.

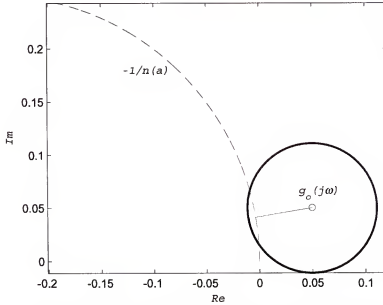


Figure 2.7. Nominal point, uncertainty value set, and critical loci for the example.

From Table 2.1 (last row, last column), the three candidate amplitudes that must be considered are

$$a_1^*(\omega) = \frac{8mg_{oi}(\omega)}{\pi\theta_1(\omega)} = -7.692$$

$$a_2^*(\omega) = \frac{8mg_{oi}(\omega)}{\pi\theta_2(\omega)} = 0.0527$$

and

$$a_3^*(\omega) = \infty$$

Noting that $d(\omega, -7.692)$ does not exist because the amplitude must be strictly positive, $d(\omega, 0.0527) = 0.0541$, and $d(\omega, \infty) = 0.5523$, it follows that the minimum distance sought is achieved at $a^* = 0.0527$. From equation (2.15) it follows that $k_N(\omega) = 1.306 > 1$. It can be concluded from Theorem 2.2 that the uncertain nonlinear closed loop system is not robustly stable with respect to the given uncertainty.

Further insight is gained from Figure 2.8, which shows a plot of the argument of the right-hand side of (2.10) as a function of the amplitude a . The infimum value ≈ 0.1280 occurs as $a \rightarrow \infty$ and the maximum value $= 1.306$ occurs at $a = 0.0527$. The numerical results are consistent with the numerical root-analysis discussed above.

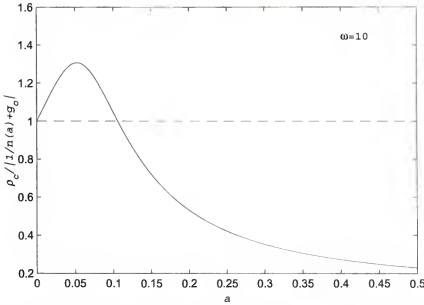


Figure 2.8. The Nyquist robust stability margin plotted versus the amplitude for the example.

2.5.2 Circular Value Set with Saturation Describing Function

Consider the open-loop stable system

$$g_o(s) = \frac{2s}{s^2 - s + 1}$$

with an associated unstructured (circular) uncertainty with radius

$$r(\omega) = \frac{2}{3} \left| \frac{j\omega}{(j\omega)^2 - j\omega + 1} \right|$$

and a nonlinear operator $f(e)$ of the form given in Figure 2.5 with $k = 3$ and $d = 2$.

The describing function in this case is given by equation (2.24). It is straightforward to show that the nominal closed-loop system is unstable.

Figure 2.9 shows the nominal point $g_o(j\omega)$ at a frequency $\omega = 0.8$, along with a circular disk representing the uncertain value set at this frequency. At this frequency,

$\rho_c(\omega, a) = r(\omega) = 0.6079$. The figure also shows the critical loci for amplitudes ranging from 0.01 to 10,000.

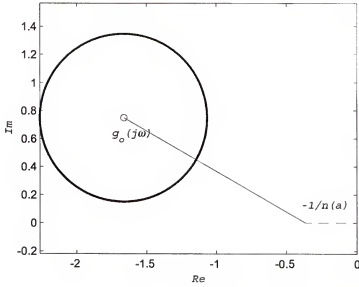


Figure 2.9. Nominal point, uncertainty value set, and critical loci for the saturation describing function.

Because the nominal point is to the left of the critical loci, the smallest distance given by (2.25) is

$$d_1^*(\omega) = \left(g_{oi}^2(\omega) + g_{or}^2(\omega) + \frac{2\pi g_{or}(\omega)}{2.3768k} + \left(\frac{\pi}{2.3768k} \right)^2 \right)^{1/2} = 1.4335$$

From equation (2.15) it follows that $k_N(0.8) = 0.4241 < 1$ so the system is robustly stabilizing at the given frequency.

However, Theorem 2.2 states that $k_N(\omega) < 1 \quad \forall \omega$ in order for the system to be robustly stable for all frequencies. Figure 2.10 shows the values of $k_N(\omega)$ calculated for a sequence of points spaced in the range $[0.001, 10]$. The maximum value of the Nyquist robust stability margin is $k_N(\omega) = 0.4241$ which occurs at a frequency $\omega = 0.8$. From

Figure 2.10 it is readily concluded that $k_N(\omega) < 1$ therefore the closed loop is robustly stable for the given uncertainty.

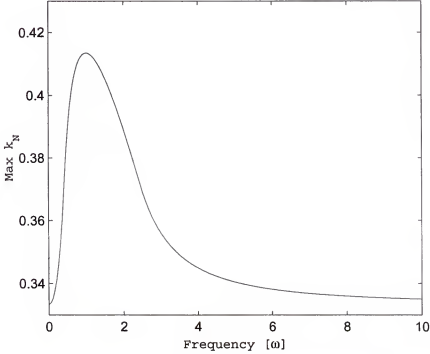


Figure 2.10. The Nyquist robust stability margin plotted versus the frequency for the saturation example.

2.5.3 Affine Uncertainty Structure with Describing Function

Consider the system with affine uncertainty structure

$$g(s, \mathbf{q}) = \frac{(0.6s^3 + 2.9s^2 + 7.5s + 15) + (0.12s^2 + 0.7s + 1)q_1 + (0.06s^2 + 0.2s)q_2 + (-0.3s - 1)q_3}{(2s^4 + 11s^3 + 30s^2 + 20s + 0.2) + (0.5s^3 + 2s^2 - s)q_1 + (-0.5s^3 + s^2)q_2 + (0.5s^3 + s)q_3}$$

where the parameter uncertainty vector belongs to the rectangular polytope

$$\mathcal{Q} = \{\mathbf{q} \in \mathbb{R}^3 \mid -10 \leq q_1 \leq 10, \quad -0.3 \leq q_2 \leq 0.3, \quad -0.3 \leq q_3 \leq 0.3\}$$

With this uncertainty the system now has a non-convex critical uncertainty value set $\nu_c(\omega)$ at the frequency $\omega = 1.6$, as can be determined by inspection of the frame $g(j\omega, \mathcal{E}(\mathcal{Q}))$ of the value set shown in Figure 2.11. The figure shows that as one travels

from the nominal point $g_o(\omega)$ in all directions spanned by the critical cone $\theta_c(\omega)$ that there are several intersections with the value set boundary. As a consequence of this geometry, the critical uncertainty value set $\nu_c(\omega)$ is a collection of lines and the unions of two disjointed line segments.

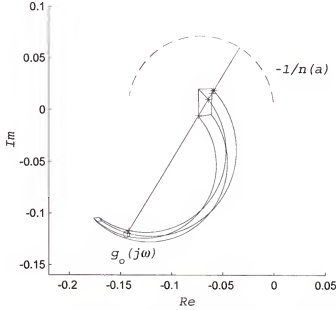


Figure 2.11. Frame for the uncertainty set for the non-convex system at the frequency $\omega = 1.6$.

Theorem 2.4 is used to determine the linear feasibility for every point belonging to the critical loci $-1/n(a)$. For a frequency $\omega = 1.6$, it can be readily verified that the problem is infeasible for all points along the critical loci. From Theorem 2.4 it follows that $-1/n(a) \notin \nu(\omega)$ and therefore it can be claimed that at $\omega = 1.6$, the value set excludes the critical loci.

The critical perturbation radius $\rho_c(\omega)$ and Nyquist robust stability margin $k_N(\omega)$ can now be calculated for any frequency using the method described by Section 2.4.2 and Baab *et al.* (2001). There are an infinite amount of directions to search inside the critical cone $\theta_c(\omega)$ and therefore only a finite amount of critical directions can be

searched. The Nyquist robust stability margin is calculated for each critical direction and the largest $k_N(\omega)$ that results is employed. Invoking equation (2.8) it is readily determined that at the frequency $\omega = 1.6$

$$k_N(1.6) = 0.7698 < 1$$

which is a result that is consistent with the conclusion reached using Theorem 2.4 that the value set does not include the critical loci at this frequency.

Figure 2.12 illustrates the values of $k_N(\omega)$ calculated for a sequence of 200 frequency points equally spaced in a logarithmic scale in the range $[0.001, 10]$.

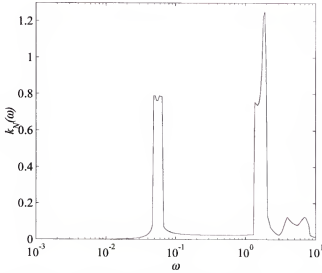


Figure 2.12. Nyquist robust stability margin $k_N(\omega)$ for the real affine parametric uncertainty system

From Figure 2.12 it is readily concluded that $k_N(\omega) > 1$ making the closed loop unstable with respect to the given uncertainty.

2.6. Conclusions and Future Work

This paper extends previous work on robustness theory for linear systems to the case of nonlinearities that can be captured through the describing function method. A new definition of the Nyquist robust stability margin for both convex and non-convex

systems takes into account a critical loci via the describing function approach is introduced. Circular value sets are studied and analytic expressions for candidate amplitudes for minimizing the Nyquist robust stability margin are derived for several nonlinear examples including the case of valve saturation. Real affine parametric uncertain systems were analyzed via a feasibility problem and arc intersections similar to Baab *et al.* (2001). Finally, three examples were given that illustrated the analytic expressions obtained and the non-convex definition of the critical perturbation radius.

CHAPTER 3

SYSTEMATIC ALGORITHMS FOR CHARACTERIZING THE ROBUSTNESS OF PREDICTIVE CONTROLLERS

3.1. Introduction

Linear models of plants used for designing predictive controllers are affected by different degrees of uncertainty that normally appear as errors in the coefficients to the numerator and denominator polynomials. Such real parametric uncertainties, although of unknown value, are often known to lie within a domain. Representative uncertainty-domain types include the cases where the domain can be described as a hyperellipsoid or as a hyperbox (*i.e.*, a rectangular polytope).

More specifically, Ellipsoidal uncertainties are defined as a vector of uncertain plant parameters that are constrained to lie inside a known ellipsoid. These descriptions are common when using regression techniques to fit experimental data to model parameters (Belforte *et al.*, 1990), and are often encountered in the context of predictive control design. These regression techniques produce a nominal value for the parameters and a variance-covariance matrix that is used to specify an ellipsoidal region centered around the nominal plant values. Ellipsoidal descriptions have the advantage that they can be quantified using systematic statistical methods, as opposed to previous unstructured uncertainty descriptions which are difficult to quantify (Kouvaritakis *et al.*, 1992; Hrisagis *et al.*, 1996) and often depict excessively conservative domains (Zafirou, 1990; Genceli and Nikolaou, 1993). Hyperbox uncertainty descriptions appear when the parameter identification procedure yields upper and lower bounds for each of the nominal

parameter coefficients. Such descriptions can also be obtained from the statistics of the parameter identification procedure, from physical arguments (for example, knowledge that the maximum error possible in the parameter is within plus or minus 10% of the nominal value).

The challenge for robust predictive control design is to find a set of tuning parameters, namely control weights and prediction horizons, that produce a stable closed loop for all the plants belonging to a given real parametric uncertainty description. This chapter presents a methodology for (i) *robust stability analysis*, i.e., determining whether a given predictive control design is robustly stabilizing with respect to the given real parametric uncertainty domain, and (ii) *robust predictive control synthesis*, i.e., finding a set of tuning parameters that ensure that the design is robustly stabilizing with respect to the given uncertainty domain. The method proposed is based on a numerical approach that allows addressing in a systematic the robustness analysis and robust synthesis problems. A numerical approach is adopted because, unlike previous robust design methodology for predictive controllers using the Youla parameter (Mahon *et al.*, 1999), the underlying optimization problems are not convex. The computational burden is nevertheless reasonable for off-line calculations, and the underlying algorithms do not require significant effort in developing software solutions because they involve standard and readily available tools, such as linear programming, for example. The approach allows the control designer to effectively identify predictive control tuning parameters that improve the robust stability of the loop.

3.2. Formulation of the Problem

3.2.1 Uncertainty Description

Consider the nominal plant transfer function

$$y(z) = \frac{B(z)}{A(z)} u(z) \quad (3.1)$$

with input $u(z)$, output $y(z)$, and with known coprime polynomials

$$A(z) = z^n + a_{n-1}z^{n-1} + \cdots + a_0$$

and

$$B(z) = b_m z^m + b_{m-1}z^{m-1} + \cdots + b_0$$

of order n and m , respectively, where $n > m$. The uncertain process model is given by the transfer function

$$y(z) = \frac{B(z) + \Delta B(z)}{A(z) + \Delta A(z)} u(z) \quad (3.2)$$

where the polynomial uncertainties

$$\Delta A(z) = \delta a_{n-1}z^{n-1} + \delta a_{n-2}z^{n-2} + \cdots + \delta a_0$$

$$\Delta B(z) = \delta b_m z^m + \delta b_{m-1}z^{m-1} + \cdots + \delta b_0$$

feature uncertain real coefficients defined by the vector

$$\delta \mathbf{p} = [\delta a_{n-1} \ \delta a_{n-2} \ \cdots \ \delta a_0 \ \delta b_m \ \delta b_{m-1} \ \cdots \ \delta b_0]^T \in \Re^{n+m+1} \quad (3.3)$$

that belongs to a known closed parametric domain Δ , i.e., $\delta \mathbf{p} \in \Delta \subset \Re^{n+m+1}$.

The generality of the approach is enhanced if the description of the uncertainty domain can be cast in the normalized form

$$\Delta = \left\{ \mathbf{t} \in \Re^{n+m+1} \mid \|\mathbf{t}\|_p \leq 1 \right\} \quad (3.4)$$

where $\|\bullet\|_p$ represents the vector p-norm. The choice of an appropriate norm depends on the uncertainty description. One case of interest is where the uncertainty domain is the ellipsoid

$$\Delta_e = \left\{ \delta \mathbf{p} \in \Re^{n+m+1} \mid \delta \mathbf{p}^T \mathbf{Q}^{-1} \delta \mathbf{p} \leq 1 \right\} \quad (3.5)$$

which is characterized by a known symmetric positive-definite matrix $\mathbf{Q} \in \Re^{(n+m+1) \times (n+m+1)}$. Introducing the coordinate transformation

$$\mathbf{t}_e := \mathbf{Q}^{-1/2} \delta \mathbf{p} \quad (3.6)$$

allows rewriting (3.5) as

$$\Delta_e = \left\{ \mathbf{t}_e \in \Re^{n+m+1} \mid \|\mathbf{t}_e\|_2 \leq 1 \right\} \quad (3.7)$$

which is in the normalized form (3.4).

A second case considered is where the uncertainty description is given as the symmetric rectangular polytope

$$\Delta_b = \left\{ \delta \mathbf{p} \in \Re^{n+m+1} \mid -\mathbf{b} \leq \delta \mathbf{p} \leq \mathbf{b} \right\} \quad (3.8)$$

which is fully characterized by the vector $\mathbf{b} \in \Re^{n+m+1}$ that contains positive elements.

The inequalities in (3.8) are interpreted to apply in an element-wise fashion. Consider the coordinate transformation

$$\mathbf{t}_b = \text{diag}(\mathbf{b})^{-1} \delta \mathbf{p} \quad (3.9)$$

where $\text{diag}(\mathbf{b}) \in \Re^{(n+m+1) \times (n+m+1)}$ is a diagonal matrix with diagonal elements $b_1, b_2, \dots, b_{n+m+1}$. Then the hyperbox domain (3.8) can be rewritten as

$$\Delta_b = \left\{ \mathbf{t}_b \in \Re^{n+m+1} \mid \|\mathbf{t}_b\| \leq 1 \right\} \quad (3.10)$$

which is of the normalized form (3.4). The transformations (3.6) and (3.9) can be represented in the generic form

$$\mathbf{t} = \mathbf{D}^{-1} \delta \mathbf{p} \quad (3.11)$$

where $\mathbf{D} = \mathbf{Q}^{1/2}$ and $\mathbf{t} = \mathbf{t}_e$ in the case where $\Delta = \Delta_e$, and $\mathbf{t} = \mathbf{t}_b$ and $\mathbf{D} = \text{diag}(\mathbf{b})$ in the case where $\Delta = \Delta_b$.

3.2.2 Robustness of Predictive Control Designs

A controller is said to be a predictive controller if at every sampling instant t it minimizes the performance functional

$$J(t) = \sum_{i=1}^{N_y} [r(t+i) - y(t+i|t)]^2 + \lambda \sum_{i=0}^{N_u} [\Delta u(t+i)]^2 \quad (3.12)$$

where $\{r(t+i)\}$ is a sequence of future setpoints, $\{y(t+i|t)\}$ is the series of future values of the output predicted at time t , and $\{\Delta u(t+i)\}$ is the sequence of future controller inputs. Tuning is achieved by selecting appropriate values for the control weighting parameter λ , the prediction horizon N_y , and the control horizon N_u .

Crisalle *et al.* (1989) have shown that the predictive controller that minimizes (3.12) can be written in a transfer- function form (see also Mahon *et al.*, 1999; Hrisagis *et al.*, 1996). More specifically, in the absence of uncertainty the plant (3.2) reduces to the nominal plant (3.1), and the control law that minimizes (3.12) is of the form

$$\frac{R(z)}{z^n} u(z) = T(z) r(z) - \frac{S(z)}{z^n} y(z) \quad (3.13)$$

where $R(z)$, $S(z)$, and $T(z)$ are controller polynomials given by

$$R(z) = z^n + r_{n-1}z^{n-1} + \dots + r_0 \quad (3.14)$$

$$S(z) = s_n z^n + s_{n-1} z^{n-1} + \dots + s_0 \quad (3.15)$$

$$T(z) = t_{N_y} z^{N_y} + t_{N_y-1} z^{N_y-1} + \dots + t_1 z \quad (3.16)$$

The controller polynomials $R(z)$, $S(z)$, and $T(z)$ are functions of the tuning parameters λ , N_y , and N_u , and of the nominal polynomials $A(z)$ and $B(z)$. Furthermore, these polynomials fulfill the requirements that $R(1) = 0$ and $T(1) = S(1)$, which guarantees the presence of an integrator in the predictive control law (Hrissagis *et al.*, 1996), and ensures that the closed loop system realizes zero offset in servo-response problems when the loop is stable. The resulting predictive control scheme is illustrated in Figure 3.1 where the controller is deployed in feedback with the uncertain plant. Details for determining the controller polynomials (3.14) – (3.16) can be found in Crisalle *et al.* (1989), Mahon *et al.* (1999), and Hrissagis *et al.* (1996).

Carrying out straightforward block-diagram algebra in Figure 3.1 for the nominal case where there is no uncertainty (*i.e.*, $\Delta A(z) = \Delta B(z) = 0$) yields the characteristic polynomial of the nominal closed loop system

$$A_0^*(z) = A(z)R(z) + B(z)S(z) \quad (3.17)$$

which can be used to assess the stability of the closed loop.

Let \mathcal{S} denote the set of all Schur polynomials (*i.e.*, the set of polynomials whose roots lie strictly inside the unit circle). The closed loop with predictive control shown in Figure 3.1 is said to be *nominally stable* if $A_0^*(z) \in \mathcal{S}$. When uncertainty is included, the uncertain characteristic polynomial is

$$A^*(z) = (A(z) + \Delta A(z))R(z) + (B(z) + \Delta B(z))S(z) \quad (3.18)$$

and the closed loop is said to be *robustly stable* if $A^*(z) \in S$ for all $\delta p \in \Delta$. A predictive controller is *robustly stabilizing* if it ensures the nominal and robust stability of the closed loop.

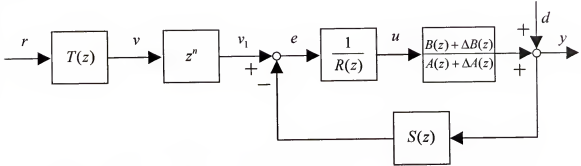


Figure 3.1. Structure of a predictive controller characterized by the operator polynomials $R(z)$, $S(z)$, and $T(z)$. The loop variables include the set point r , the input u , and the exogenous disturbance d .

A scalar measure of the robust stability of the closed loop is given by the parametric stability margin

$$\alpha = \left\{ \min_{t \in R^{n+1}} \|t\|_p \mid A^*(z) \notin S \right\} \quad (3.19)$$

where $\|\bullet\|_p$ represents the vector p -norm and where $t = t_e$ for the case $\Delta = \Delta_e$, and $t = t_b$ for the case $\Delta = \Delta_b$. The parameter α is interpreted as the size of the smallest destabilizing parameter perturbation. Note that if $\alpha > 1$, the size of the smallest destabilizing parametric uncertainty is $\|t\|_p = \alpha > 1$. Given that the set Δ includes only uncertain parameter vectors whose size is $\|t\|_p \leq 1$, it follows that no element of Δ is destabilizing. Hence, when $\alpha > 1$ the predictive control loop is robustly stable with respect to all uncertainties in the set Δ . Conversely, when $\alpha \leq 1$, there is at least one element of Δ that is destabilizing, and the predictive control loop is not robustly stable with respect to Δ . The choice of p -norm in (3.19) depends on the structure of the

parametric uncertainty domain Δ . Obviously, the 2-norm is used to analyze the case of the ellipsoidal uncertainty domain (3.7) and the ∞ -norm to treat the hyperbox domain (3.10).

3.3. Computation of the Parametric Stability Margin

The focus for the robust stability analysis is the characteristic equation

$$A^*(z) = 0, \text{ or equivalently}$$

$$\Delta A(z)R(z) + \Delta B(z)S(s) = -A_0^*(z) \quad (3.20)$$

which is obtained after setting (3.18) equal to zero, rearranging terms, and using the definition of $A_0^*(z)$ given in (3.17). The analysis of robust stability requires the characterization of the parametric uncertainty set that places the closed-loop poles on the unit circle $z = e^{j\omega}$, $\omega \in [0, \pi]$, namely, the set that satisfies $A^*(e^{j\omega}) = 0$ for some values of frequency. Using a vector-matrix representation of equation (3.20), the key to the robust stability analysis is to identify vectors $\delta \mathbf{p}$ that satisfy

$$\mathbf{c}^T(z)\delta \mathbf{p} = -A_0^*(z) \quad (3.21)$$

where

$$\mathbf{c}(z) := \begin{bmatrix} z^{n-1}R(z) & z^{n-2}R(z) & \cdots & R(z) & z^m S(z) & z^{m-1}S(z) & \cdots & S(z) \end{bmatrix}^T$$

and where $z = e^{j\omega}$. Furthermore, using the normalizing transformation (3.11), equation (3.21) can be written as

$$\mathbf{c}^T(z)\mathbf{D}\mathbf{t} = -A_0^*(z)$$

and the calculation of the parametric robust-stability margin (3.19) then reduces to solving the frequency-dependent program

$$\alpha(\omega) = \left\{ \min_{\mathbf{t} \in \mathfrak{R}^{++++}} \|\mathbf{t}\|_p \mid \mathbf{c}^T(e^{j\omega})\mathbf{D}\mathbf{t} = -A_0^*(e^{j\omega})\mathbf{c}^T(e^{j\omega})\mathbf{D}\mathbf{t} = -A_0^*(e^{j\omega}) \right\} \quad (3.22)$$

and then setting

$$\alpha = \left\{ \min_{\omega \in [0, \pi]} \alpha(\omega) \right\}$$

3.3.1 Ellipsoidal Uncertainty

When the uncertainty is constrained to lie within the ellipsoid (3.7), equation (3.21) can be expressed as

$$\mathbf{c}_e^T(z)\mathbf{t}_e = -A_0^*(z)$$

where $\mathbf{c}_e^T(z) = \mathbf{c}^T(z)\mathbf{Q}^{1/2}$, and where \mathbf{t}_e is defined in (3.6). Adopting the 2-norm in the definition of the parametric stability margin leads to an optimization problem of the form (3.22) as follows:

$$\alpha(\omega) = \left\{ \min_{\mathbf{t}_e \in \mathfrak{R}^{++++}} \|\mathbf{t}_e\|_2 \mid \mathbf{c}_e^T(e^{j\omega})\mathbf{t}_e = -A_0^*(e^{j\omega}) \right\} \quad (3.23)$$

The solution to the standard linear-quadratic problem (3.23) is given by analytical expression

$$\mathbf{t}_{e,\min} = \frac{-A_0^*(e^{j\omega})}{\mathbf{c}_e^T(e^{j\omega})\mathbf{c}_e(e^{j\omega})} \mathbf{c}_e(e^{j\omega})$$

so that

$$\alpha(\omega) = \|\mathbf{t}_{e,\min}\|_2$$

Obviously, the uncertain system is robustly stable if and only if $\alpha = \min_{\omega \in [0, \pi]} \alpha(\omega) > 1$. It is

interesting to note that

$$\alpha(0)^2 = B(1)^2 \phi \quad (3.24)$$

where

$$\phi = \frac{1}{\rho(m+1)} \quad (3.25)$$

for the case where the domain (3.5) is a sphere with radius ρ , and for the case of an arbitrary ellipsoid

$$\phi = \frac{\left\| \sum_{i=1}^n \mathbf{q}_{RS,i} \right\|_2^2 + \left\| \sum_{i=1}^{m+1} \mathbf{q}_{SS,i} \right\|_2^2}{\left(\sum_{i=1}^{m+1} \sum_{k=1}^{m+1} \mathbf{Q}_{SS,ik} \right)^2} \quad (3.26)$$

where the submatrices $\mathbf{Q}_{RR} \in \mathfrak{R}^{n \times n}$, $\mathbf{Q}_{SR} \in \mathfrak{R}^{(m+1) \times n}$, $\mathbf{Q}_{RS} \in \mathfrak{R}^{n \times (m+1)}$, and

$\mathbf{Q}_{SS} \in \mathfrak{R}^{(m+1) \times (m+1)}$ are extracted from the partition

$$\mathbf{Q} := \begin{bmatrix} \mathbf{Q}_{RR} & \mathbf{Q}_{RS} \\ \mathbf{Q}_{SR} & \mathbf{Q}_{SS} \end{bmatrix}$$

and the vectors \mathbf{q}_i^{RS} and \mathbf{q}_i^{SS} for $i = 1, 2, \dots, m+1$ are extracted from the partitions

$$\mathbf{Q}_{RS}^{1/2} := \begin{bmatrix} \mathbf{q}_1^{RS} & \mathbf{q}_2^{RS} & \dots & \mathbf{q}_{m+1}^{RS} \end{bmatrix}, \quad \mathbf{Q}_{SS}^{1/2} := \begin{bmatrix} \mathbf{q}_1^{SS} & \mathbf{q}_2^{SS} & \dots & \mathbf{q}_{m+1}^{SS} \end{bmatrix}$$

When the ellipsoid is a sphere characterized by $\mathbf{Q} = \rho \mathbf{I}$, $\rho > 0$, then $\mathbf{Q}_{RS} = \mathbf{0}$ and $\mathbf{Q}_{SS} = \rho \mathbf{I}$, and hence (3.26) reduces to (3.25).

It is interesting to note that $\alpha(0)$ is constant and is dependent only on the plant zeros. The robust stability of the system at the frequency $\omega = 0$, therefore, may be altered by changing the zeros of the nominal plant.

3.3.2 Hyperbox Uncertainty

Constraining the uncertainty to lie within the hyperbox (3.8), and adopting the ∞ -norm in the definition of the parametric stability margin, it is possible to proceed as in Section 3.3.1 to formulate the following optimization problem of the form (3.22):

$$\alpha(\omega) = \left\{ \min_{\mathbf{t}_b \in \mathcal{R}^{\text{uncert}}} \|\mathbf{t}_b\|_{\infty} \mid \mathbf{c}_b^T(e^{j\omega})\mathbf{t}_b = -A_0^*(e^{j\omega}) \right\} \quad (3.27)$$

where

$$\mathbf{c}_b^T(e^{j\omega}) := \mathbf{c}^T(e^{j\omega}) \text{diag}(\mathbf{b})$$

The optimization problem (3.27) has been formulated following the development in Bhattacharya (1995), where it is shown that a solution can be computed effectively using readily available linear-programming algorithms. The solution $\mathbf{t}_{b,\min}$ is such that

$$\alpha(\omega) = \|\mathbf{t}_{b,\min}\|_{\infty}$$

Obviously, the system is robustly stable if

$$\alpha = \min_{\omega \in [0, \pi]} \alpha(\omega) > 1$$

In contrast to the ellipsoidal case, an analytical expression for $\alpha(0)$ cannot be readily obtained because, in general, the problem does not afford an analytical solution.

3.4. Robustification of Predictive Controllers

Two different controllers are examined: (i) a standard predictive controller (SPC) design that ignores uncertainty (*i.e.*, $\Delta A(z) = \Delta B(z) = 0$) and that is based on equations (3.13) – (3.16) and (ii) a robust predictive controller (RPC) that stabilizes the loop for all plants lying within a given uncertainty set Δ . The performance of each controller is evaluated via simulation for both a servo and regulation test for the closed loop uncertain

system. The robustification process consists of analyzing the effect of the tuning parameters λ , N_y , and N_u on the robust stability margin α . Only those tuning parameters that ensure that $\alpha > 1$ are accepted as robustly-stabilizing choices, provided that such choices also ensure the nominal stability of the loop.

3.4.1 Ellipsoidal Uncertainty

Consider the stable nominal plant model

$$\frac{B(z)}{A(z)} = \frac{z - 0.3}{z^2 - 0.8 + 0.16} \quad (3.28)$$

with the ellipsoidal parametric uncertainty description (3.5) characterized by

$$\mathbf{Q} = \begin{bmatrix} 0.1000 & 0.0490 & 0.0140 & 0.0105 \\ 0.0490 & 0.0700 & 0.0275 & 0.0130 \\ 0.0140 & 0.0275 & 0.1200 & -0.0208 \\ 0.0105 & 0.0130 & -0.0208 & 0.0600 \end{bmatrix}$$

A standard predictive controller is designed with tuning parameters $N_y = 4$,

$N_u = 2$, and $\lambda = 0$, resulting in the following controller polynomials:

$$R(z) = z^2 - 1.2920z + 0.2920$$

$$S(z) = 1.7900z^2 - 0.9487z + 0.1558$$

$$T(z) = -0.1578z^4 - 0.0106z^3 + 0.2905z^2 + 0.8750z$$

The SPC controller stabilizes the nominal system because the characteristic polynomial

$$A_0^*(z) = z^4 - 0.3021z^3$$

has all its roots inside the unit circle. The methodology of

Section 3.3.1 is used to characterize the robustness of the SPC design, yielding a

parametric stability margin, $\alpha = 0.8833 < 1$. Hence, this design is not robustly

stabilizing, and it can be concluded that there are plants in the ellipsoidal domain for

which the closed loop is unstable.

Figure 3.2 illustrates the results of SPC closed loop simulations with both a nominal and perturbed plant. The uncertain coefficient vector considered is

$$\delta p = [0.0971 \quad -0.0093 \quad 0.2470 \quad -0.1599]^T$$

which corresponds to the perturbed plant

$$\frac{B(z) + \Delta B(z)}{A(z) + \Delta A(z)} = \frac{1.2470z - 0.4599}{z^2 - 0.7029z + 0.1507}$$

The coefficient vector is included in the ellipsoidal domain because $\delta p^T Q \delta p = 0.9714 < 1$. The SPC design is tested via servo and regulation tests by making a setpoint change at $t = 75$ and introducing a persistent step disturbance $d(t) = 1$ at $t = 25$. The SPC stabilizes the loop of the nominal plant, but produces an unstable closed loop for the perturbed plant, causing unbounded input and output signals. Therefore, the standard predictive controller is not acceptable from the robust-stability viewpoint and it must be redesigned.

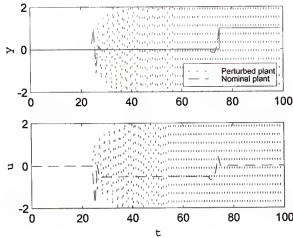


Figure 3.2. Ellipsoidal uncertainty example. Closed loop responses of the SPC design considered in the example to a set point change and to an exogenous disturbance injection.

A robust predictive controller (RPC) is designed by first calculating the value of the robust stability margin, α using the numerical method discussed in Section 3.1 over a range of the control-weighting parameter, namely $0 \leq \lambda \leq 10$. The prediction and control horizons are kept at the same values used by the SPC design, namely, $N_y = 4$ and $N_u = 2$. It is straightforward to verify that for all the values of λ considered, the poles of $A_0^*(z)$ lie strictly in the unit circle. Therefore, all values $0 \leq \lambda \leq 10$ are nominally stabilizing. The results are shown in Figure 3.3, where the parametric stability margin initially increases sharply, reaching a maximum value of $\alpha = 1.715$ at $\lambda = 0.6$. All values of λ in Figure 3.3 that result in $\alpha > 1$ ensure robust stability. Note that Figure 3.3 shows that all designs with $\lambda \leq 0.0413$ are not robustly stabilizing. Using Figure 3.3, the weighting parameter is selected as $\lambda = 0.6$ for maximum stability robustness. The resulting maximally robust RPC design is then tuned using $\lambda = 0.6$, $N_y = 4$, and $N_u = 2$.

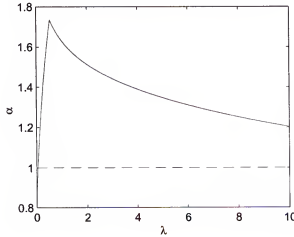


Figure 3.3. Ellipsoidal uncertainty example. Effect of the control-weighting parameter λ on the parametric stability margin α . The values of α located above the horizontal dashed line correspond to robustly stabilizing weighting-parameter values.

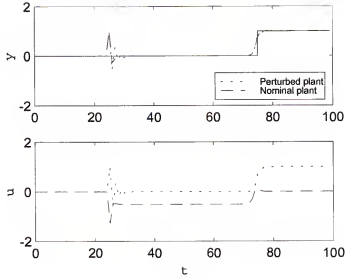


Figure 3.4. Ellipsoidal uncertainty example. Closed loop responses of the RPC design considered in the example to a set point change and to an exogenous disturbance injection.

The RPC design stabilizes the nominal plant since the resulting nominal characteristic polynomial $A_0^*(z) = z^4 - 0.7921z^3 + 0.2724z^2 - 0.0386z$ is Schur given that its zeros are located at $\{0, 0.2380 \pm 0.2556j, 0.3161\}$. The RPC design is also robustly stabilizing because $\alpha = 1.715$. Figure 3.4 illustrates the RPC simulation results for the nominal and perturbed plant using the same servo and regulation tests performed earlier. Note that the RPC design produces adequate output responses, effectively tracking the setpoint and rejecting the disturbance for both the nominal and the perturbed plant.

3.4.2 Hyperbox Uncertainty

Consider the nominal plant (3.28) with an associated hyperbox uncertainty of the form (3.8) where

$$\mathbf{b} = [0.2 \quad 0.2 \quad 0.2 \quad 0.2]^T$$

As in the previous example, two controller designs, denoted as SPC and RPC are evaluated for robust stability and performance.

The SPC tuning parameters chosen are $N_y = 4$, $N_u = 2$, and $\lambda = 0.1$. The closed loop under SPC control is nominally stable because the characteristic polynomial $A_0^*(z) = z^4 - 0.4528z^3 + 0.0831z^2 - 0.0116z$ has all roots inside the unit circle. Using the linear-programming method discussed in section 3.3.2, it's readily determined that the robust stability of the SPC design has a parametric robust-stability margin $\alpha = 0.5942 < 1$. Therefore, the SPC design is not robustly stabilizing with respect to the hyperbox uncertainty considered.

Given that $\alpha < 1$ for the SPC design, it is anticipated that the closed loop must be unstable for some plants in the uncertainty domain. Consider the coefficient vector $\delta\mathbf{p} = [0.1701 \quad -0.1701 \quad 0.1701 \quad -0.1701]^T$ in the hyperbox domain, which results in the perturbed plant

$$\frac{B(z) + \Delta B(z)}{A(z) + \Delta A(z)} = \frac{1.701z - 0.4701}{z^2 - 0.6299 - 0.0101}$$

Figure 3.5 illustrates that the SPC controller stabilizes the nominal plant, but produces an unstable response for the perturbed plant. A more robust controller must be designed.

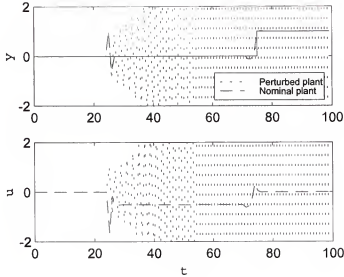


Figure 3.5. Hyperbox uncertainty example. Closed loop responses of the SPC design considered in the example to a set point change and to an exogenous disturbance injection.

The RPC is designed taking advantage of the effect of λ the parametric stability margin, α , as illustrated in Figure 3.6 where the horizons are fixed at $N_y = 4$ and $N_u = 2$. It is straightforward to verify that all values of λ considered (namely $0 \leq \lambda \leq 10$) produce nominally stabilizing predictive control designs (*i.e.*, the resulting $A_0^*(z)$ are Schur). The parametric stability margin increases sharply from $\lambda = 0$ to $\lambda = 2.7$ where it realizes its maximal value $\alpha = 1.626$. Any λ that results in $\alpha \geq 1$ ensures robust stability with respect to the given uncertainty set. The choice $\lambda = 2.7$ corresponds to the RPC design with maximal robust stability. Note that all weighting parameter choices $\lambda \leq 0.3825$ fail to deliver a robustly stabilizing design because $\alpha \leq 1$.

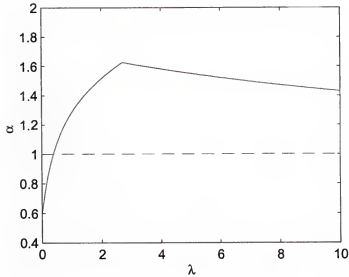


Figure 3.6. Hyperbox uncertainty example. Effect of the control-weighting parameter λ on the parametric stability margin α . The values of α located above the horizontal dashed line correspond to robustly stabilizing weighting-parameter values.

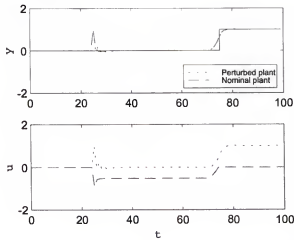


Figure 3.7. Hyperbox uncertainty example. Closed loop responses of the RPC design considered in the example to a set point change and to an exogenous disturbance injection.

The RPC is designed using the tuning parameters $N_y = 4$, $N_u = 2$, and $\lambda = 2.7$.

Robust stability is ensured because $\alpha = 1.626 > 1$. Nominal stability is also attained

given that the characteristic polynomial $A_0^*(z) = z^4 - 1.1048z^3 + 0.4588z^2 - 0.0673z$ is

Schur because its zeros are $\{0, 0.3849 \pm 0.2297j, 0.3349\}$. Figure 3.7 illustrates that the RPC stabilizes the closed loop featuring either the nominal or the perturbed plant.

3.5. Conclusions

This chapter presents an approach to analyze robust predictive controllers based on a parametric stability margin that can be computed numerically using well-known algorithms. The parametric stability margin offers a quantitative measure of robust stability that destabilizes the system, and serves as a basis for the efficient robustification of predictive controller designs. Two types of parametric uncertainty descriptions, namely ellipsoidal and hyperbox, are treated in detail. The systematic algorithms proposed allow the user to determine the effect of a tuning parameter on the robust stability of the system. Although the examples focused on the effect of the control-weighting parameter λ , an analogous procedure can be used to analyze the effects of the control horizons N_u and N_y .

CHAPTER 4 PREDICTIVE CONTROL OF A WASTEWATER TREATMENT PLANT

4.1 Introduction

Government regulations require wastewater treatment plants to disinfect water before it is discharged to the environment. This can be accomplished in a variety of methods, but the most common process is to add chlorine to reduce the harmful compounds (Metcalf & Eddy, 1979). Chlorine reacts in this process and regulations necessitate a minimum level of chlorine concentration and minimum residence time upon leaving the reactor. This ensures that enough chlorine is present to provide satisfactory cleansing (Hammer and Hammer, 1996). However, high chlorine levels are harmful for three reasons: (1) chlorine is a significant operating cost, (2) unnecessary addition of chlorine means that greater volumes must be stored on-site, and (3) high chlorine concentrations tend to form trihalomethane (THM) contaminants (Jolley *et al.*, 1990). Therefore the controller design cannot allow high concentrations of chlorine and must maintain the outlet chlorine concentration at the desired set point.

The objective of this research is to develop an effective chlorine control scheme to overcome the technological challenges associated with a wastewater treatment plant. Plants have little storage space for water; thus they must process water as it arrives and are subject to large cyclical demands for water (Hammer and Hammer, 1996). This change in water flow causes a time-varying delay, due to the reactor's size being fixed, and is a considerable challenge for process control of wastewater (Smith, 1971). There are other lesser disturbances such as intense solar radiation (causing increases in

volatilization of chlorine, evaporation of water, and chemical reaction rates) and rainfall (causing dilution) that can affect the dynamics of outdoor reactors.

Several feedback control strategies have been developed throughout the years to provide optimal outlet chlorine concentration levels with varying results. The simplest method is applying a proportional-integral (PI) controller in a cascade feedback form, but this usually fails for systems with large disturbances and time delays (Seborg *et. al.*, 1989). The addition of a Smith Predictor, requiring an accurate model of the system, can reduce the effects of time delays if the delay is relatively static (Ogunnaike and Ray, 1994). These two methods fail to control a system with very high disturbances or time delays as are present in wastewater treatment plants. Meredith (2003) found an effective technique by modifying the reactor with a dynamic weir which allows the controller to manipulate the residence time of the water in the reactor by changing the reactor volume. This modification essentially makes the time delay of the system constant and has been found to be extremely effective in controlling chlorine concentration. However this requires a physical modification to the wastewater treatment plant.

Many advanced control strategies require accurate models of the process in order to be effective. A schematic of the general design of wastewater treatment plants is shown below in Figure 4.1. The wastewater enters the dosing area where chlorine is added to eliminate ammonia nitrogen from the water (Metcalf & Eddy, 1979). The ammonia is quickly removed in this basin and the reactions can be described by the Morris-Wei model (Morris and Wei, 1969). However the Morris-Wei model introduces a combination of algebraic and differential equations which increase the computational

burden. A simplification was developed by Snoeyink and Jenkins (1980) that assumes a first order model and greatly simplifies the computation.

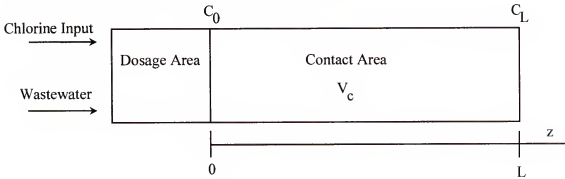


Figure 4.1. Schematic of wastewater treatment plant

The outflow from the dosing area then enters the contact area where most of the disinfection takes place. This area of the reactor is modeled as a series of continuous stirred tank reactors (CSTR) in series. For more information on the model please see Meredith (2003) and Bierck *et al* (1996). Meredith found that the optimal number of CSTRs that best modeled the plug flow reactor was 100. The model that was used in this study for the development of predictive controllers and to assess the performance of the different designs was co-developed by Demir (2001) and Meredith (2003).

This chapter reports on the development of a disturbance predictive controller that was developed. In section 4.2 the derivation of the control law is illustrated with all pertinent equations. Section 4.3 illustrates the difference between the responses of a disturbance predictive controller and predictive controller employed with both a linear and nonlinear model. Finally, 4.4 details some future directions and control schemes that may be useful.

4.2 Derivation of Disturbance Predictive Controller

The derivation of the disturbance predictive control law follows a similar form as shown by Crisalle *et al.* (1989). Consider the nominal plant transfer function

$$y(t) = \frac{B(q^{-1})}{A(q^{-1})}u(t-1) + \frac{C(q^{-1})}{D(q^{-1})}d(t) \quad (4.1)$$

with input $u(t-1)$, output $y(t)$, disturbance $d(t)$, and known coprime polynomials $A(q^{-1})$ and $B(q^{-1})$. Multiply both sides of (4.1) by $A(q^{-1})$ and $D(q^{-1})$ to yield

$$D(q^{-1})A(q^{-1})y(t) = D(q^{-1})B(q^{-1})u(t-1) + A(q^{-1})C(q^{-1})d(t) \quad (4.2)$$

and multiply (4.2) by $E_i(q^{-1})\Delta q^i$

$$\begin{aligned} E_i(q^{-1})D(q^{-1})A(q^{-1})\Delta y(t+i) &= E_i(q^{-1})D(q^{-1})B(q^{-1})\Delta u(t+i-1) \\ &+ E_i(q^{-1})A(q^{-1})C(q^{-1})\Delta d(t+i) \end{aligned} \quad (4.3)$$

where q^i is the forward shift operator and $\Delta = 1 - q^{-1}$. Define

$$A_d(q^{-1}) = D(q^{-1})A(q^{-1})$$

and consider the following Diophantine equation

$$1 = E_i(q^{-1})A_d(q^{-1})\Delta + q^{-i}F_i(q^{-1})$$

The Diophantine equation is used to separate the future values of $y(t+i)$ from the past values stored in $y(t)$. Rearranging the above equation yields

$$E_i(q^{-1})A_d(q^{-1})\Delta = 1 - q^{-i}F_i(q^{-1}) \quad (4.4)$$

Equation (4.4) is substituted into (4.3) to separate $y(t)$ and $y(t+i)$ resulting in

$$y(t+i) - F_i(q^{-1})y(t) = E_i(q^{-1})D(q^{-1})B(q^{-1})\Delta u(t+i-1) + E_i(q^{-1})A(q^{-1})C(q^{-1})\Delta d(t+i) \quad (4.5)$$

Next, the past and future values of the input must be similarly separated using the Diophantine equation by introducing the following polynomials

$$\Gamma_i(q^{-1}) = \gamma_{i,0} + \gamma_{i,1}q^{-1} + \dots + \gamma_{i,n_i-1}q^{-n_i+1}$$

$$G_i(q^{-1}) = g_0 + g_1q^{-1} + \dots + g_{i-1}q^{-i+1}$$

and requiring $\Gamma_i(q^{-1})$ and $G_i(q^{-1})$ to satisfy

$$E_i(q^{-1})B_d(q^{-1}) = G_i(q^{-1}) + q^{-i}\Gamma_i(q^{-1}) \quad (4.6)$$

where

$$B_d(q^{-1}) = D(q^{-1})B(q^{-1})$$

To separate the input values substitute (4.6) into (4.5)

$$y(t+i) = G_i(q^{-1})\Delta u(t+i-1) + \Gamma_i(q^{-1})\Delta u(t-1) + E_i(q^{-1})A(q^{-1})C(q^{-1})\Delta d(t+i) + F_i(q^{-1})y(t)$$

and make the following definitions for $y^{OL}(t+i)$ and $y^d(t+i)$

$$y^{OL}(t+i) = \Gamma_i(q^{-1})\Delta u(t-1) + F_i(q^{-1}) \quad (4.7)$$

$$y^d(t+i) = E_i(q^{-1})A(q^{-1})C(q^{-1})\Delta d(t+i) \quad (4.8)$$

The equations for $y^{OL}(t+i)$ and $y^d(t+i)$ are utilized later in the development of the control law.

The disturbance predictive control law is derived from the following cost function

$$J(u) = \sum_{i=1}^{N_1} [r(t+i) - y(t+i|t)]^2 + \lambda \sum_{i=0}^{N_2} [\Delta u(t+i)]^2 \quad (4.9)$$

where $r(t+i)$ are the future values of the set point, $y(t+i|t)$ are the predicted future values of the system evaluated at time t , and $\Delta u(t+i)$ are the future values of the inputs.

Rewriting (4.9) in vector-matrix form yields

$$J(u) = (\mathbf{y} - \mathbf{r})^T (\mathbf{y} - \mathbf{r}) + \lambda \mathbf{u}^T \mathbf{u} \quad (4.10)$$

Define the output of the system as

$$\mathbf{y} = \mathbf{G}\Delta \mathbf{u} + \mathbf{y}^{OL} + \mathbf{y}^d$$

and substitute into (4.10)

$$J(u) = \left(\mathbf{G}\Delta\mathbf{u} + \mathbf{y}^{\text{OL}} + \mathbf{y}^{\text{d}} - \mathbf{r} \right)^T \left(\mathbf{G}\Delta\mathbf{u} + \mathbf{y}^{\text{OL}} + \mathbf{y}^{\text{d}} - \mathbf{r} \right) + \lambda \mathbf{u}^T \mathbf{u} \quad (4.11)$$

Define the initial input as

$$\mathbf{u}_0 = \mathbf{r} - \mathbf{y}^{\text{OL}}$$

and simply (4.11) to yield

$$J(u) = \left(\mathbf{u}_0 - \mathbf{G}\Delta\mathbf{u} - \mathbf{y}^{\text{d}} \right)^T \left(\mathbf{u}_0 - \mathbf{G}\Delta\mathbf{u} - \mathbf{y}^{\text{d}} \right) + \lambda \mathbf{u}^T \mathbf{u} \quad (4.12)$$

Take the derivative of equation (4.12) to produce

$$\frac{\partial J(u)}{\partial \mathbf{u}} = -\mathbf{u}_0^T \mathbf{G} + \mathbf{u}^T \mathbf{G}^T \mathbf{G} + \mathbf{y}^{\text{d}T} \mathbf{G} + \lambda \mathbf{u}^T = 0 \quad (4.13)$$

Solving (4.13) for \mathbf{u}

$$\mathbf{u} = \left[\mathbf{G}^T \mathbf{G} + \lambda \mathbf{I} \right]^{-1} \mathbf{G}^T \left[\mathbf{r} - \mathbf{y}^{\text{OL}} - \mathbf{y}^{\text{d}} \right]$$

and rewriting yields

$$\Delta u(t) = \mathbf{k}^T \left[\mathbf{w}(t) - \mathbf{y}^{\text{OL}}(t+i) - \mathbf{y}^{\text{d}}(t+i) \right] \quad (4.14)$$

where

$$\mathbf{w}(t+i) = q^i \mathbf{r}(t)$$

$$\mathbf{k}^T = [1 \ 0 \ \dots \ 0] \mathbf{K}$$

and

$$\mathbf{K} = \mathbf{G}_L^+$$

where \mathbf{G}_L^+ is the truncated dynamic matrix.

Next, put equation (4.14) in summation form

$$\sum_{i=0}^{N_s} \Delta u(t+i) = \sum_{i=1}^{N_s} k_i w(t+i) - \sum_{i=1}^{N_s} k_i y^{\text{OL}}(t+i) - \sum_{i=1}^{N_s} k_i y^{\text{d}}(t+i) \quad (4.15)$$

and substitute (4.7) and (4.8) into (4.15) to yield the control law

$$\begin{aligned} \left[1 + q^{-1} \sum_{i=1}^{N_s} k_i \Gamma_i(q^{-1}) \right] \Delta u(t) &= \sum_{i=1}^{N_s} k_i q^i r(t) - \sum_{i=1}^{N_s} k_i F_i(q^{-1}) y(t) \\ &\quad - \sum_{i=1}^{N_s} k_i E_i(q^{-1}) A(q^{-1}) C(q^{-1}) \Delta d(t+i) \end{aligned} \quad (4.16)$$

The control law described by equation (4.16) can be expressed as $R(z)$, $S(z)$, $T(z)$, and $V(z)$ polynomials defined as

$$R(z) = z^n \left[1 + z^{-1} \sum_{i=1}^{N_s} k_i \Gamma_i(z^{-1}) \right] \Delta$$

$$S(z) = z^n \left[\sum_{i=1}^{N_s} k_i F_i(z^{-1}) \right]$$

$$T(z) = \sum_{i=1}^{N_s} k_i z^i$$

$$V(z) = \sum_{i=1}^{N_s} k_i E_i(z^{-1}) A(z^{-1}) C(z^{-1}) \Delta$$

and is illustrated in graphical form below in Figure 4.2.

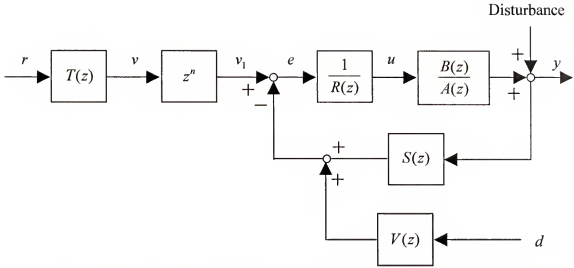


Figure 4.2. Structure of a disturbance predictive controller characterized by the operator polynomials $R(z)$, $S(z)$, $T(z)$, and $V(z)$.

4.3 Simulation of Wastewater Treatment Plants

In this section, the predictive control law developed by Crisalle *et al.* (1989) is compared to the disturbance predictive controller developed in section 4.2. Each controller is connected to the model developed by Meredith (2003) and the closed loop response obtained. In section 4.3.1, a linear, first order plus deadtime model is used as an approximation of the highly nonlinear wastewater treatment plant and utilized as an initial test system for the comparison of the two controllers is illustrated. The controller parameters discovered during the linear model simulations are used to control the nonlinear model of the wastewater treatment plant discussed in section 4.3.2

4.3.1 Closed-Loop Response of Linear Model

Figure 4.3 shows the performance of the predictive control system developed by Crisalle *et al.* (1989) applied to the linear plant model when the flowrate is modeled as sinusoidal wave, which is chosen to approximate a smooth, cyclical water consumption profile of a typical day. The sine wave begins at time 6 hr, its period is 24 hr, and the amplitude is three-fourths of the nominal flowrate ($0.4 \text{ m}^3/\text{s}$), or $0.3 \text{ m}^3/\text{s}$. The result is a

disturbance flowrate that varies from $0.1 \text{ m}^3/\text{s}$ to $0.7 \text{ m}^3/\text{s}$. These values are chosen because they represent a 7:1 ratio of maximum-to-minimum flowrate.

The linear plant is controlled with unacceptable performance, experiencing fluctuations in the output chlorine concentration. The sinusoidal flow of the amplitude described above severely degrades the quality of the controller performance for simulations of the linear plant. Figure 4.3 shows that the deviation output concentration values are as high as 1.27 ppm and as low as -1.45 ppm which would correlate to 3.27 ppm and 0.55 ppm if the set point was 2 ppm. The lower value, 0.55 ppm of chlorine, is unacceptable because it is below the level of 1 ppm established by the EPA.

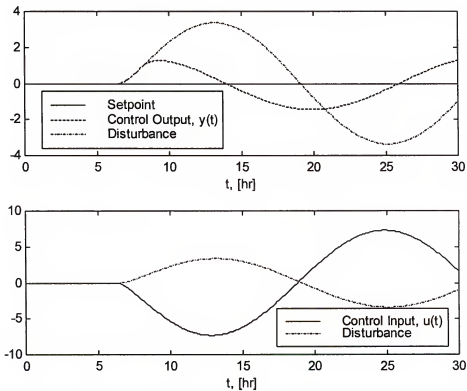


Figure 4.3. Predictive control of linear wastewater treatment plant to a sinusoidal disturbance

The disturbance predictive controller developed in section 4.2, however, does an excellent job of maintaining the outlet chlorine concentration as illustrated in Figure 4.4. The sinusoidal flow of the amplitude described above does not degrade the quality of the controller performance for simulations of the linear plant. Figure 4.4 shows that the deviation output concentration values are only as high as 0.29 ppm and as low as -0.26 ppm which would correlate to 2.29 ppm and 1.74 ppm if the set point was 2 ppm. Both of these values are well within the regulations established by the EPA demonstrating the improvement in controller performance if the disturbance predictive control scheme is utilized.

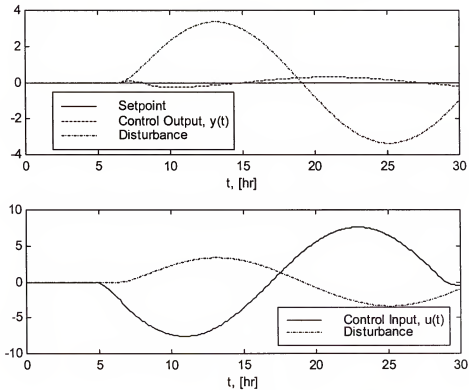


Figure 4.4. Disturbance predictive control of linear wastewater treatment plant to a sinusoidal disturbance

4.3.2 Closed-Loop Response of Nonlinear Model

The physical wastewater treatment plant is a highly nonlinear process with very different dynamics than those seen in the linear model. In Figure 4.5 a disturbance predictive controller is connected to the nonlinear model of the wastewater treatment plant. The sinusoidal disturbance is the same as used in section 4.3.1 and results in an outlet value of chlorine concentration of 0.3 ppm and 5.9 ppm. These upper and lower values are not allowable by the EPA rendering the disturbance predictive controller unacceptable for use in the highly nonlinear wastewater treatment plants.

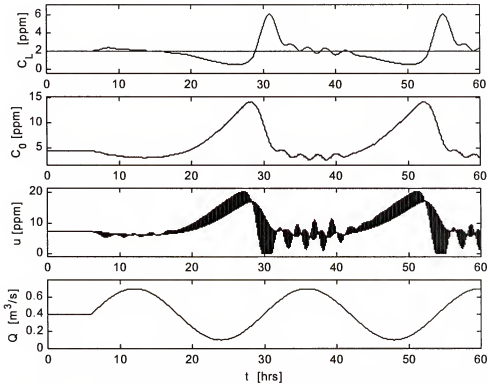


Figure 4.5. Closed-Loop response of nonlinear model with a disturbance predictive controller subjected to a varying flow

4.4 Conclusions and Future Work

The disturbance predictive controller developed is similar in structure and nature to previous predictive controllers. However it needs an accurate model of the system in

question as well as the disturbance in order to be effective. The controller is linear in form and does an excellent job if the system to be controlled is linear as illustrated in section 4.3.1. However if the system is highly nonlinear, such as a wastewater treatment plant, with very large disturbances, the disturbance predictive controller fails. One solution is to design an adaptive disturbance predictive controller similar in form to that described by Landau (1998). However, this would be very numerically intensive as the control law polynomials need to be updated often. A more practical and effective approach would be to develop a nonlinear predictive controller. This would allow the controller to maintain a strict chlorine concentration despite the large disturbances.

CHAPTER 5

AN EXCESS VOLUME MODEL TO DETERMINE CONVERSION IN AN EMULSION POLYMERIZATION REACTOR

5.1 Introduction

Emulsion polymerization became commercialized in the 1930s and has grown to become the major process for the production of synthetic polymers (Blackley, 1975). Much of this development was generated by the loss of natural rubber during World War II. Postwar, the wide spread usage of water based paints expanded emulsion polymerization processes to include acrylic resins and synthetic elastomers. Presently, many different types of polymers are produced by emulsion polymerization primarily through batch reactors. However, continuous stirred tank reactors are more commonly utilized due to economic and process advantages (Gilbert, 1995).

There is a lack of data on emulsion polymerization reactors available in literature. This slow development of polymerization reactors is due to the difficulty in developing sensors that can monitor important polymer properties on-line (Schork and Ray, 1980; Schork and Ray, 1987).

Density is measured on-line through the use of a densitometer, a vibrating U-shaped tube which continuously has liquid flowing through it. The first important work concerning on-line densitometry was performed by Canegallo *et al.* (1993) where thermal instability and coalescence of monomer droplets was analyzed and a phase separator introduced before the sample stream enters the densitometer. This phase separator

improves density measurements by removing the gas from the liquid sample to be analyzed.

Schork and Ray (1981, 1983) were the first to measure conversion on-line by developing an equation that related density to conversion with an emphasis on emulsion polymerization. They assumed that in an emulsion polymerization reaction all volumes of the components were additive and verified their experimental results with gravimetric analysis. Ponnuswamy (1986) improved the equation by comparing densitometry and GC analysis of data and was able to greatly improve the estimate of the conversion.

A large effort is currently underway to development on-line sensors to monitor the emulsion polymerization process. Guinot *et al.* (2000) performed a comparative study and analyzed the strengths and weaknesses of many sensors such as IR, NIR, and polymer reaction calorimetry. Vara (2000) improved the densitometer measurements and analyzed such issues as thermal instability for a wide variety of polymerization processes. This chapter takes the work begun at the University of South Florida by Vara and improves the conversion calculations through the use of an excess volume model. Numerical issues in root finding are addressed and several examples are presented.

5.2 Motivation

A realistic model for describing the specific volume of a mixture of polymer and its monomer in an emulsion polymerization reactor is of the form

$$v(x) = v_{0\%} + (v_{100\%} - v_{0\%})x + v^{ex}(x) \quad (5.1)$$

$$v^{ex}(x) = v(x) - (v_{0\%} + (v_{100\%} - v_{0\%})x)$$

where x is the degree of conversion of monomer, $v(x)$ is the specific volume of the mixture at the given conversion level x , $v_{0\%}$ is the specific volume of the monomer at 0% conversion, $v_{100\%}$ is the specific volume of polymer at 100% conversion, and $v^{ex}(x)$ is the

excess volume of mixing. Equation (5.1) can be interpolated as the thermodynamic equation for the volume of a mixture, and is based on the Lewis-Randall rule to select the standard states as $v_{0\%}$ and $v_{100\%}$.

The specific volume of an emulsion can be determined by measuring the density ρ of a sample and then invoking the relationship

$$v(x) = \frac{1}{\rho}$$

Given that the variable $v(x)$ can be measured, in principle, it is possible to solve (5.1) for the remaining unknown variable, namely, the degree of conversion x . Experimental work carried out by Vara assumed that the excess volume of mixing is negligible (i.e., $v^{ex}(x)=0$), and succeeded in obtaining experimental values of degree of conversion through the expression

$$x = \frac{v(x) - v_{0\%}}{v_{100\%} - v_{0\%}} \quad (5.2)$$

Vara compared the results obtained in this fashion with the trustworthy degree-of-conversion v values obtained via gravimetric analysis, and found that the approach (5.2) underestimates the degree of conversion. The conclusion that can be inferred from these observations is that it is necessary to take into account the excess volume of mixing term in (5.1) for improved accuracy in the estimation of the degree of conversion.

An example of the motivation behind the excess volume modeling is illustrated in Figure 5.1. The linear relationship between conversion and specific volume, as shown by equation (5.2), is plotted and called the ideal model ($v^{id}(x)$). The actual specific volume is shown by the curve $v(x)$ and, in this case, lies above the ideal model. Therefore, if a specific volume measurement is made, the ideal model will result in a much smaller

conversion value than is present in the reactor. Consequently, an excess volume model will significantly improve conversion calculations.

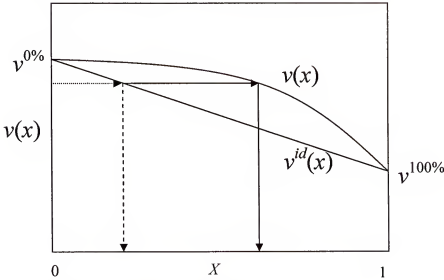


Figure 5.1. Motivation for use of an excess volume model

In this chapter, a one-parameter model and two-parameter model for the excess volume of mixing are proposed. The choice of this model depends on the shape of the excess volume. For example, if the excess volume is symmetric, a one-parameter model may be used.

5.3 One-Parameter Excess Volume Model

5.3.1 Mathematical Formulation

For a symmetric excess volume, the following one-parameter model is proposed:

$$v^{ex}(x) = A_I x(1 - x) \quad (5.3)$$

where the parameter A_I must be determined experimentally. The parameter A_I can be defined as the excess volume coefficient. The one-parameter model assumes that the dependence of $v^{ex}(x)$ on x is symmetric in the conversion range $[0, 1]$; however, this assumption must be verified experimentally. If through further experimental studies it is

determined that excess volume curve is asymmetric, then a two-parameter model can be considered.

From (5.3) it follows that the maximum absolute value of the excess volume is realized at 50% conversion (i.e., $x=0.5$). Defining $v_{50\%}^{ex} := v^{ex}(0.5)$, it follows that

$$v_{50\%}^{ex} = A_1 0.5(1 - 0.5) = \frac{A_1}{4}$$

Or, equivalently,

$$A_1 = 4v_{50\%}^{ex}$$

Therefore, the modeling parameter A_1 can be interpreted as the excess volume of mixing at 50% conversion multiplied by a factor of 4.

Note that $v^{ex}(x)$ (and therefore the parameter A_1) must be a function of the molecular weight distribution of the polymer. Analogously, the variable $v_{100\%}$ also depends on the molecular weight distribution. Throughout these developments it is assumed that both A_1 and $v_{100\%}$ are weak functions of the molecular weight distribution, as is implicitly assumed by equation (5.2).

Substituting the model (5.3) into the specific volume expression (5.1) yields the corrected specific volume equation

$$v(x) = v_{0\%} + (v_{100\%} - v_{0\%})x + A_1 x(1 - x) \quad (5.4)$$

or

$$v(x) = v_{0\%} + (v_{100\%} - v_{0\%} + A_1)x - A_1 x^2$$

5.3.2 Determining the Excess Volume Parameter

The excess volume parameter A_1 can be obtained from an experimental value of conversion x_i determined from gravimetric analysis and from the corresponding value of

specific volume $v(x_i)=1/\rho(x_i)$ obtained using a densitometer measurement. Substituting both of these experimental values in (5.4) and rearranging terms gives the expression

$$-A_1 x_1 (1 - x_1) = v_{0\%} - v(x_1) + (v_{100\%} - v_{0\%}) x_1 \quad (5.5)$$

which can be readily solved for the unknown to yield

$$A_1 = -\frac{v_{0\%} - v(x_1) + (v_{100\%} - v_{0\%}) x_1}{x_1 (1 - x_1)} \quad (5.6)$$

The experimental conversion value x_1 must be selected away from the extreme values of $x=0$ and $x=1$ where excess volume model (5.3) vanishes, rendering equation (5.6) invalid.

A better method for obtaining an experimental value for A_1 is by least-squares regression using a finite number of experimental conversion data x_i and a corresponding set of specific volume data $v(x_i)$, $i=1, 2, \dots, N$. As discussed earlier, the experimental points should be chosen far away from the extreme values of $x_i=0$ and $x_i=1$. The data are then used to pose the following set of N equations patterned after equation (5.5):

$$\begin{aligned} -A_1 x_1 (1 - x_1) &= v_{0\%} - v(x_1) + (v_{100\%} - v_{0\%}) x_1 \\ -A_1 x_2 (1 - x_2) &= v_{0\%} - v(x_2) + (v_{100\%} - v_{0\%}) x_2 \\ &\vdots \\ -A_1 x_N (1 - x_N) &= v_{0\%} - v(x_N) + (v_{100\%} - v_{0\%}) x_N \end{aligned}$$

Finally, the system of equations is readily solved in the least-squares sense to give the parameter estimate

$$A_1 = -\frac{\sum_{i=1}^N x_i (1 - x_i) [v_{0\%} - v(x_i) + (v_{100\%} - v_{0\%}) x_i]}{\sum_{i=1}^N x_i^2 (1 - x_i)^2} \quad (5.7)$$

Clearly, equation (5.7) reduces to (5.6) when $N=1$.

5.3.3 Solving the One-Parameter Quadratic Equation

The specific volume equation (5.4) can be solved for the degree of conversion x when an experimental value of specific volume is available. Rearranging terms in (5.4) yields the second-order polynomial equation

$$A_1 x^2 - (v_{100\%} - v_{0\%} + A_1)x + (v(x) - v_{0\%}) = 0$$

with roots

$$x^{(1)} = \frac{v_{100\%} - v_{0\%} + A_1}{2A_1} - \frac{\sqrt{(v_{0\%} - v_{100\%} - A_1)^2 - 4A_1(v(x) - v_{0\%})}}{2A_1}$$

$$x^{(2)} = \frac{v_{100\%} - v_{0\%} + A_1}{2A_1} + \frac{\sqrt{(v_{0\%} - v_{100\%} - A_1)^2 - 4A_1(v(x) - v_{0\%})}}{2A_1}$$

or

$$x^{(1)} = \left(\frac{1}{2} + \frac{v_{100\%} - v_{0\%}}{2A_1} \right) - \sqrt{\left(-\frac{1}{2} + \frac{v_{0\%} - v_{100\%}}{2A_1} \right)^2 - \frac{v(x) - v_{0\%}}{A_1}} \quad (5.8)$$

$$x^{(2)} = \left(\frac{1}{2} + \frac{v_{100\%} - v_{0\%}}{2A_1} \right) + \sqrt{\left(-\frac{1}{2} + \frac{v_{0\%} - v_{100\%}}{2A_1} \right)^2 - \frac{v(x) - v_{0\%}}{A_1}} \quad (5.9)$$

Therefore, the degree of conversion x will be given by either $x = x^{(1)}$ or $x = x^{(2)}$.

Further studies are needed to determine how one should select one of the two available roots as a solution to the conversion problem. One case where the problem is easily resolved is when one of the roots lies inside the interval $[0, 1]$ and the other root lies outside. In this case the selection is straightforward because the solution must satisfy $0 \leq x \leq 1$; hence, one simply chooses the root that lies inside the $[0, 1]$ interval.

A second case that is more complicated arises should both roots lie inside the interval $[0, 1]$. Consider for example the case where a density value $\rho = \rho_{100\%}$ is measured at an instant when the reactor has reached 100% conversion. It then follows that

$v(x)=1/\rho_{100\%}=v_{100\%}$; substituting this quantity into (5.8) and (5.9) and carrying out simple manipulation yields

$$x^{(1)} = \left(\frac{1}{2} + \frac{v_{100\%} - v_{0\%}}{2A_1} \right) - \sqrt{\left(\frac{1}{2} + \frac{v_{0\%} - v_{100\%}}{2A_1} \right)^2} \quad (5.10)$$

$$x^{(2)} = \left(\frac{1}{2} + \frac{v_{100\%} - v_{0\%}}{2A_1} \right) + \sqrt{\left(\frac{1}{2} + \frac{v_{0\%} - v_{100\%}}{2A_1} \right)^2} \quad (5.11)$$

or

$$x^{(1)} = \left(\frac{1}{2} + \frac{v_{100\%} - v_{0\%}}{2A_1} \right) - \left(\frac{1}{2} + \frac{v_{0\%} - v_{100\%}}{2A_1} \right) = \frac{v_{0\%} - v_{100\%}}{A_1}$$

$$x^{(2)} = \left(\frac{1}{2} + \frac{v_{100\%} - v_{0\%}}{2A_1} \right) + \left(\frac{1}{2} - \frac{v_{100\%} - v_{0\%}}{2A_1} \right) = 1$$

If $0 < (v_{0\%} - v_{100\%})/A_1 < 1$, then it would be difficult to discern between the correct answer $x=x^{(2)}=1$ and the alternative answer $x=x^{(1)} = (v_{0\%} - v_{100\%})/A_1$ because both roots lie in the interval $[0, 1]$. Further research must be carried out to determine if the condition

$0 < (v_{0\%} - v_{100\%})/A_1 < 1$ is physically meaningful (for example, this case would not be relevant if physical arguments can be used to show that $(v_{0\%} - v_{100\%})/\gamma < 0$, effectively eliminating the root $x^{(1)}$). A more comprehensive study of the roots in this case will be necessary, particularly taking into consideration the sign of A_1 .

A third case of relevance is a situation where both roots $x(1)$ and $x(2)$ lie outside the interval $[0, 1]$. Such roots are meaningless, but such a situation could conceivably arise if the densitometer produces an incorrect measurement located outside the range $[\rho_{100\%}, \rho_{0\%}]$. Although this outcome is hypothetical, it should be ruled out as a possibility to ensure the robust performance of the degree-of-conversion prediction. Perhaps this

problem can be dealt with easily by introducing upper and lower saturation values on the acceptable output of the densitometer.

A final concern that must be taken into account is that for systems where A_I is small (i.e., the excess volume is negligible) the formula (5.2) must be used in lieu of formulas (5.10)–(5.11). Note that the equations (5.10)–(5.11) fail in this case due to the appearance of the parameter A_I in the denominator, causing unacceptable division-by-zero errors when the parameter is either zero or very small.

5.4 Redlich-Kister Two-Parameter Model

5.4.1 Mathematical Formulation

If the experimental excess volume is determined to be asymmetric, a two-parameter model must be implemented. The following model is proposed:

$$v^{ex}(x) = Ax(1-x) + Bx(1-x)(2x-1) \quad (5.12)$$

where the parameters A and B must be determined experimentally. This model does not assume that $v^{ex}(x)$ must be symmetric in the conversion range $[0, 1]$.

The two-parameter model adds another level of complexity in the determination of the model coefficients and conversion values. There are no useful analytical expressions for determining A and B as there were with the one-parameter model. However, the same assumptions (that A , B , and $v_{100\%}$ are weak functions of the molecular weight distribution) are used in the Redlich-Kister model as well.

Substituting the two-parameter model (5.12) into the specific volume expression (5.1) yields the corrected specific volume equation

$$v(x) = v_{0\%} + (v_{100\%} - v_{0\%})x + Ax(1-x) + Bx(1-x)(2x-1) \quad (5.13)$$

5.4.2 Determining the Excess Volume Parameters

Using the Redlich-Kister model adds a degree of difficulty to the analysis. The coefficients A and B have no simple analytical solutions. Instead, least-squares regression must be used and be of the form $y = Ax$ with a solution $x = (A^T A)^{-1} A^T y$ where

$$y = \begin{bmatrix} V_{ex}(1) \\ \vdots \\ V_{ex}(n) \end{bmatrix} \quad A = \begin{bmatrix} x_1(1-x_1) & x_1(1-x_1)(2x_1-1) \\ \vdots & \vdots \\ x_n(1-x_n) & x_n(1-x_n)(2x_n-1) \end{bmatrix} \quad x = \begin{bmatrix} A \\ B \end{bmatrix}$$

Therefore if $B=0$ then the Redlich-Kister model reduces to the one-parameter model.

5.4.3 Solving the Redlich-Kister Cubic Equation

The specific volume equation (5.13) can be solved for the degree of conversion x when the specific volume is available. A third-order polynomial results when the terms in (5.13) are rearranged

$$x^3 + \left(-\frac{3B-A}{2B}\right)x^2 + \left(-\frac{A+v_{100\%}-v_{0\%}-B}{2B}\right)x + \left(-\frac{v_{0\%}-v(x)}{2B}\right) = 0$$

The three roots for this expression can be numerically solved to yield the degree of conversion.

Further study is needed to determine how to select one of the three roots as a solution to the problem. The easiest case is when one roots lies in the interval $[0, 1]$ and the other two lie outside the interval. In this case, the root in the interval $[0, 1]$ is chosen.

A second case that is more complicated occurs when one of the roots is real and two are complex conjugates of each other. This occurs when $D>0$ where

$$D = -\frac{1}{46656} \frac{(6Bv_{100\%} - 6Bv_{0\%} + B^2 + A^2)^3}{B^6} + \left[\frac{(3B - A)}{24B^2} (A + v_{100\%} - v_{0\%} - B) + \frac{v_{0\%} - v(x)}{4B} + \frac{(3B - A)^3}{216B^3} \right]^2 \quad (5.14)$$

Therefore, there are two manners in which $D > 0$. First, because of the squared term in equation (5.14), D will be greater than zero if

$$\left[\frac{(3B - A)}{24B^2} (A + v_{100\%} - v_{0\%} - B) + \frac{v_{0\%} - v(x)}{4B} + \frac{(3B - A)^3}{216B^3} \right]^2 > \frac{1}{46656} \frac{(6Bv_{100\%} - 6Bv_{0\%} + B^2 + A^2)^3}{B^6}$$

which will guarantee that there is only one root. An alternative condition involves evaluating the cubed term in equation (5.14). In order for $D > 0$, the cubic term in (5.14) must be negative. Thus, the following condition must hold

$$6Bv_{100\%} - 6Bv_{0\%} + B^2 + A^2 < 0$$

Rearranging terms and solving for $v_{0\%} - v_{100\%}$ results in the expression

$$\frac{A^2 + B^2}{6B} < v_{0\%} - v_{100\%} \quad (5.15)$$

From the physical analysis of the emulsion system, it can be shown that the quantity $v_{0\%} - v_{100\%}$ is positive. Therefore if the A and B coefficients adhere to the preceding expressions, solving for the degree of conversion will result in only one real root.

5.5 Example – Polymerization of Styrene

5.5.1 Development of Models

An experimental emulsion polymerization apparatus at the University of South Florida was used to obtain gravimetric and density data versus time for the polymerization of

styrene. The gravimetric data are used as the “correct” value for the conversion in the reactor. Using the density data obtained versus time and equation (5.2), the uncorrected value of conversion was calculated and compared to gravimetric results in Figure 5.2.

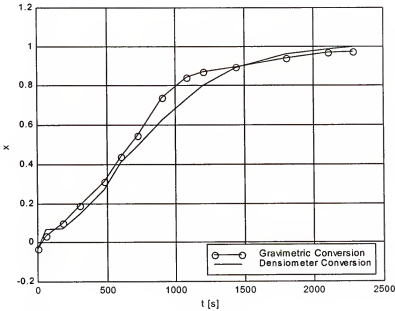


Figure 5.2. Comparison of gravimetric and densitometer conversion versus time

As illustrated in Figure 5.2, the gravimetric and densitometer conversions diverge by as much as 0.15 from 0.4 to 0.8 conversion. An excess volume model must be used.

The experimental excess volume is calculated by solving equation (5.1) for $v^{ex}(x)$. A one-parameter model is then necessary to improve the densitometer conversion calculations. A least-squares regression is performed to obtain the excess volume parameter A_1 , as shown in section 5.2.2. The experimental excess volume is then compared to the one-parameter model for $v^{ex}(x)$ in Figure 5.3. The one-parameter model is symmetric and reaches a maximum at 0.5 conversion while the experimental v^{ex} is not symmetric and reaches a maximum around 0.75 conversion. A two-parameter model would yield a better result due to the asymmetric excess volume.

In order to obtain the parameters A and B , a least-squares regression is performed as illustrated in Section 5.3.2. The Redlich-Kister model is shown in Figure 5.3 and is compared to the experimental excess volume and the one-parameter model. The two-parameter model is a better fit for the asymmetric experimental excess volume. However, the model still predicts a higher excess volume between 0.3 and 0.6 and underestimates the excess volume between 0 and 0.3 as well as 0.6 to 0.9.

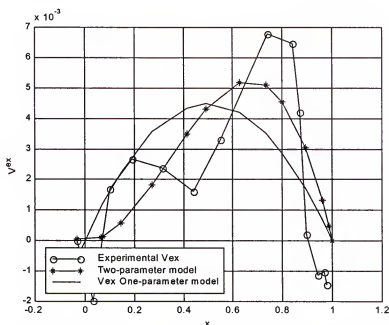


Figure 5.3. Experimental v^{ex} and v^{ex} one-parameter model versus conversion

5.5.2 Conversion Calculations

In Figure 5.4, the conversion values are calculated for both the one- and two-parameter models and plotted versus time. Both excess volume models improve the conversion calculations; however, there are still questions associated with each.

There are still some issues concerning the one-parameter model. First, at conversions from 0.2 to 0.6, the conversion calculated for the one-parameter model is actually greater than for the gravimetric conversion. This is because the $v^{ex}(x)$ model

yields a higher excess volume than is shown through experimentation. In addition, the model predicts less conversion between 0.6 and 0.8 than is reported through gravimetric determination. A two-parameter model may be able to correct these inaccuracies.

The Redlich-Kister model is then used as the excess volume model and the resulting cubic equation is solved for the conversion. Two of the roots must be eliminated in order to solve for the proper value of conversion. For the polymerization of styrene, equation (5.15) holds true, making two of the roots imaginary. The resulting real root is the value for the conversion and is compared to the one-parameter model and gravimetric conversion in Figure 5.4.

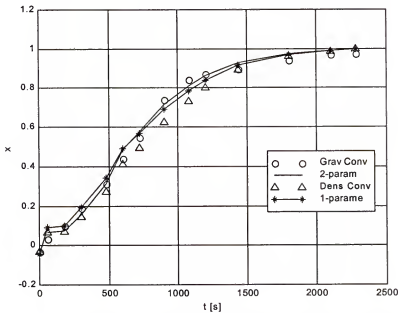


Figure 5.4. Conversion curves for different excess volume models compared to gravimetric and densitometer conversion

As illustrated above, the two-parameter model provides a more accurate value for conversion than the one-parameter model or the densitometer. However, at conversions around 0.4 to 0.5, both the one- and two-parameter model report a conversion higher than the actual conversion determined by gravimetric methods for reasons discussed

previously. Possible solutions are to add another parameter which would lead to a fourth-order equation in terms of conversion and may not be practical to solve.

5.6 Copolymerization of Styrene and Butyl-Methacrylate

5.6.1 Development of Models

The excess volume model is determined by taking the difference between the gravimetric and densitometer conversion at different conversions. The experimental and theoretical excess volume models are illustrated in Figure 5.5. Because there was no data obtained for conversions below 0.5, it is anticipated that the theoretical models will be inaccurate over the entire conversion range. It is also impossible to determine if the excess volume is symmetric over the entire conversion range. It can be seen in Figure 5.5 that neither of the two models accurately fit the experimental data.

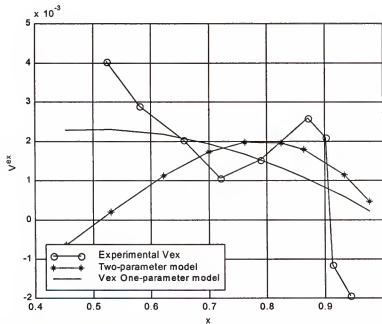


Figure 5.5. Experimental and theoretical excess volume versus conversion

5.6.2 Conversion Calculations

The one- and two-parameter models are used to improve the conversion calculations shown in Figure 5.6. The one-parameter model does a better job of matching the gravimetric conversion than the two-parameter model except between 0.8 and 0.9.

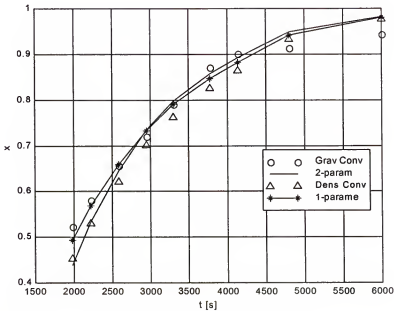


Figure 5.6. Conversion versus time for different models

This conclusion could change, however, with the addition of both densitometer and gravimetric conversions between 0 and 0.5. The excess volume may turn out to be symmetric throughout the conversion range, allowing the two-parameter model to be more accurate. More experimentation is required.

5.7 Polymerization of Butyl-Methacrylate

5.7.1 Development of Models

The excess volume model is determined by taking the difference between the gravimetric and densitometer conversion at different conversions. The experimental and theoretical excess volume models are illustrated in Figure 5.7. The shape of the

experimental excess volume is not symmetric and the shape does not match any of the available shapes from the one- and two-parameter models. Both the one- and two-parameter models do not agree with the experimental data. It is possible that the models may actually decrease the accuracy of the conversion calculations.

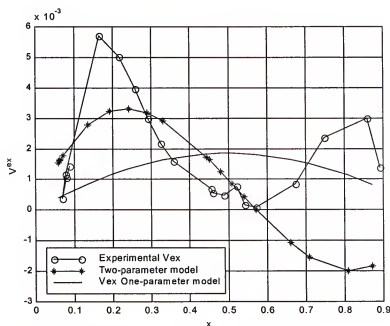


Figure 5.7. Experimental and theoretical excess volume

5.7.2 Conversion Calculations

In Figure 5.8, the gravimetric, densitometer, and excess volume conversion calculations are plotted versus time. In this example, the densitometer conversion is actually more accurate than the conversions determined with the one- and two-parameter models. Both the one- and two-parameter models diverge from the gravimetric conversion at some point during the reaction.

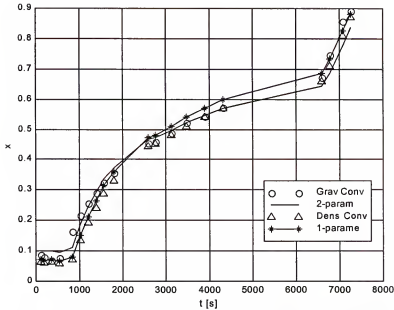


Figure 5.8. Conversion calculation for different models and methods

5.8 Conclusions

In this chapter, it has been shown that it is possible to determine the conversion of an emulsion polymerization reaction by measuring the density of the emulsion over time. The density is inversely proportional to the specific volume of the emulsion reaction. The conversion of the reaction can then be measured on-line with the use of a densitometer.

There are differences, however, between the conversion determined by gravimetric analysis and the conversion calculated by the densitometer. This difference can be modeled through the use of an excess volume model. The model can take many mathematical forms; the two that are used here involved both a one- and two-parameter model.

Deciding which model to use is the critical design problem. The model chosen must be able to guarantee that a conversion root will be found inside 0 and 1.0. Different polymers may yield different results and may require that a certain model is used in order to ensure a correct conversion calculation.

It has been shown above that this methodology can be applied to several polymerization reactions. The two-parameter model was best suited to styrene while the one-parameter model was used in the copolymerization reaction. It was even illustrated with butyl-methacrylate that sometimes not using an excess volume model is the only practical solution. The methodology described works and is effective for an emulsion polymerization reaction.

CHAPTER 6 DESIGN AND CONTROL OF A CONTINUOUS SAMPLING AND DILUTION SYSTEM

6.1. Introduction

6.1.1 Motivation Behind the CSDS

In recent years, real time monitoring of chemical processes has become very important in both academia and industry. On-line monitoring of process conditions such as concentration, pressure, or temperature is highly desirable in order to design an effective control scheme (Sacoto 1999). On-line monitoring allows for improved product quality that would not be possible through off-line techniques. For example, real-time monitoring allows improvements in the resolution of data.

Real-time measurements are practically impossible as there is always an associated time lag with the steps between sampling and obtaining the desired data. Regardless, real-time conditions can be approached if the correct sensing strategy is utilized.

There are four different types of strategies that were considered for this process: off-line, on-line, in-line, and in-situ. Each strategy has advantages and disadvantages. Off-line requires taking a sample and performing the analysis after the experiment has concluded. On-line sampling takes a sample and analyzes it while the experiment is still running while in-line sampling introduces a sensor within the process itself. In-situ monitoring is the least invasive of the four techniques as it places a sensor around the experiment.

Although on-line sampling methods do not approach real-time measurements as much as in-line or in-situ measurements, they do have one main advantage. On-line methods can use existing sensors with the fewest modifications while in-line and in-situ measurements require expensive and very specialized probes. In addition, on-line sensing is very similar to the off-line strategy making the data interpretation similar. Because of the reasons stated above, the on-line strategy was employed in this project.

With a appropriate sampling and dilution, much of today's most commonly used sensing equipment can be modified to monitor chemical processes on-line (Sacoto 1999). In the area of concentrated dispersions, defined as highly concentrated solutions, many researchers have attempted to monitor composition and particle properties. For example, emulsion polymerization researchers have often measured polymer conversion on-line through the use of a densitometer (Canegallo, *et. al*, 1993; Moritz, *et. al*, 1985) or free surfactant concentration from surface tension (Schork and Ray, 1983). Additionally there is a great deal of research in the area of on-line measurements of particle size and particle size distribution (Elicabe and Garcia-Rubio, 1988; Kourti *et. al.*, 1984). Many of these techniques require, or would be greatly improved by, some type of dilution system.

This chapter reports on the design, implementation, and control of a continuous sampling and dilution system (CSDS) developed at the University of South Florida for on-line monitoring of concentrated dispersions.

6.1.2 Issues of CSDS Monitoring

There are a number of challenges associated with on-line dilution systems. Included among these challenges are: representative sampling, time delay associated with dilution, and sample integrity. This section covers each of these problems in turn.

Representative sampling involves finding a suitable sampling location, the optimal number of samples, and discovering a suitable amount of sample required to perform the analysis. Locating a suitable sampling location is crucial since a well-mixed vessel is not necessarily uniformly distributed. For example, in a continuous stirred tank reactor non-ideal mixing yields dead zones while in concentrated dispersions the size distribution, surface charge, or density may introduce dead zones (Sacoto, 1999). If the sampling location is chosen in a dead zone the sample is not representative of the entire reactor. One solution to this problem is to sample from several locations but the added cost and complexity associated with this development may be too high.

Depending on the dilution required, on-line sampling may require large amounts of sample which would adversely affect the system, *i.e.* a process disturbance. If the dilution is to be continuous, then large amounts of waste will be generated. Because many techniques, light scattering or chromatography for example, require large dilutions this becomes a serious problem. For UV-VIS spectrometry a dilution factor of five to six orders of magnitude is required (Sacoto, 1996). Thus, for a given dilution step 10 to 100 liters of diluent is required for every milliliter of sample (Sacoto, 1999). The diluted sample does not return to the experimental process, resulting in 10 to 100 liters of waste per milliliter of sample analyzed.

Time delay, or transport delay, is also of critical importance. If the dilution is performed in steps (as in the CSDS) then each dilution step increases the time delay and biases the interpretation of the data. The time delay is often seen to increase the error in the estimation of particle concentration and particle size distribution (Elicabe and Garcia-Rubio, 1988). There are two major effects observed as the time delay increases: (1) a

shift in time relative to the sample populations present and (2) an averaging of the data over the measurement interval and a loss in resolution.

The sample integrity must be preserved from the time the sample is taken from the reactor to the time it is analyzed. This may be of critical importance depending on the composition of the dispersion. For example, a change in the continuous phase will affect the equilibrium of the system; an alteration in the chemical potential will force other phases to be altered to keep equilibrium. Thus, the components within the system would be redistributed and the sample analyzed by the sensor would be significantly different from what originally left the reactor. For example, in emulsion polymerization polymer particles and monomer droplets are present, but when diluted the monomer droplets disappear. The particle size distribution and distribution of monomer within the particles would then be biased and the measurement inaccurate.

6.1.3 Novelty of the CSDS

There have been many types of dilution systems developed throughout the years. A system developed by Nicoli and Elings (1989) consists of a series of dilution steps through stirred tanks and differential pressure for sampling as shown in Figure 6.1. A sample is taken from the experimental reactor and passed into the first CSTR where it is diluted. A second sample is taken from the first CSTR and passed into a second CSTR where it is diluted again. The process is repeated n times until the final sample is sent to the sensor. The design is continuous in nature, but very large amounts of diluent are required and there are time distribution problems involved with the continuous stirred tank reactors (CSTR).

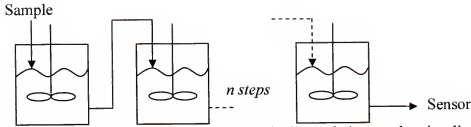


Figure 6.1. Dilution system proposed by Nicoli *et. al.* that can be visualized as a sequence of CSTR in series.

Ponnuswamy and Shah (1986) compiled various analytical measurements carried both off- and on-line to monitor polymer quality in a batch polymerization reactor. White (1994) designed a dilution system that is on-line but does not have continuous sampling and dilution using various solvent and sample vessels for multiple dilutions. Most previous work on dilution systems does not have continuous sampling and/or has time distribution problems associated with it.

6.2 Design and Implementation of CSDS

6.2.1 General design

A continuous sampling and dilution system developed at the University of South Florida consists of a tubing network of interconnected sampling and dilution lines that run parallel to each other as shown in Figure 6.2. The process begins when a sample is taken from the reactor and mixed with a line carrying diluent. The sample and diluent are then allowed to mix over a designated tube length while static mixers are added to increase radial mixing and ensure a homogeneous bulk concentration. A sample is then taken from the first dilution line and pumped to a second dilution channel creating a second dilution step. The dilution process is repeated n times.

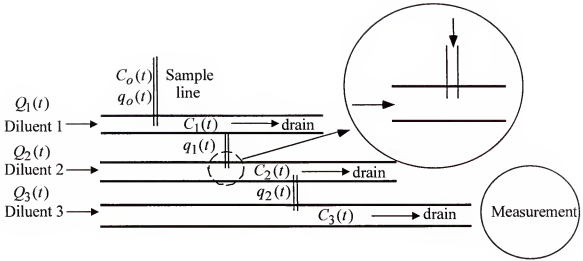


Figure 6.2. Schematic of the CSDS with three dilution steps

The premise behind the continuous sampling and dilution system is to choose the diluent flow rates, $Q_i(t)$, to be significantly larger than the sample flow rates, $q_{i-1}(t)$, where i is the number of dilution steps. Sacoto (1999) derived the following steady state equation for concentration

$$C_i(t) = \frac{C_{i-1}(t)q_{i-1}(t)}{Q_i(t) + q_{i-1}(t)}$$

where $C_i(t)$ corresponds to the overall sample concentration at the i^{th} step. It should be noted that if $Q_i(t) > q_i(t)$ it will lead to very high dilution ratios. However, this equation only analyzes one dilution step; for multiple steps these equations need to be combined to determine the end concentration.

There are many advantages to using the continuous sampling and dilution system as opposed to other dilution systems such as the system developed by Nicoli and Elings (1989). The CSDS, unlike some previously designed systems, does not suffer from age distribution problems because the CSDS can be modeled as several plug flow reactors in series.

The CSDS is a modular system; extra dilution steps may be added or removed easily. If the dispersion is highly concentrated, it may be necessary to add a step. This has the adverse effect of increasing the dilution time, *i.e.*, the time from when the sample is taken to when the sample is analyzed by the spectrometer. However, even with several dilution steps, the time lag is on the order of 5 minutes.

Next, the dilution times are short, roughly 5 or 6 minutes (Sacoto, 1999), which allows faster, more accurate control. Finally, the CSDS can be used continuously, which makes it a potentially powerful tool for process control.

6.2.2 The Dynamic Model of the CSDS

In order to implement advanced control strategies (such as a Smith predictor or model predictive control) an accurate model of the system must be developed. A first principles model is derived below and is used for simulation and controller design. The derivation begins by performing a mass balance on the first stage of the dilution system

$$\frac{d(V_1 C_1)}{dt} = Q_1(t)C + q_0(t)C_0(t) - q_1(t)C_1(t) - Q_{l_0}(t)C_1(t) \quad (6.1)$$

There is no product in the dilution line, thus $C = 0$. Q_{l_0} is defined as

$$Q_{l_0}(t) = Q_1(t) + q_0(t) - q_1(t)$$

Plugging this expression into equation (6.1) yields

$$\frac{d(V_1 C_1)}{dt} = q_0(t)C_0(t) - q_1(t)C_1(t) - (Q_1(t) + q_0(t) - q_1(t))C_1(t)$$

The terms $q_1(t)C_1(t)$ cancel each other out leaving the following equation

$$\frac{d(V_1 C_1)}{dt} = q_0(t)C_0(t) - (Q_1(t) + q_0(t))C_1(t)$$

Because the volume is constant in the dilution system, it can be factored out of the integral and simplified to result in

$$\frac{d(C_1)}{dt} = \frac{q_0(t)}{V_1} C_0(t) - \frac{(Q_1(t) + q_0(t))}{V_1} C_1(t) \quad (6.2)$$

Equation (6.2) is then checked against the steady state model developed by Sacoto (1999) shown below

$$C_1(t) = \frac{C_0(t)q_0(t)}{Q_1(t) + q_0(t)}$$

The derivative in equation (6.2) is set equal to zero in order to calculate a steady state solution and rearranged to give

$$\frac{q_0(t)}{V_1} C_0(t) = \frac{(Q_1(t) + q_0(t))}{V_1} C_1(t) \quad (6.3)$$

The volumes cancel each other and equation (6.3) can be rearranged to yield

$$C_1(t) = \frac{C_0(t)q_0(t)}{Q_1(t) + q_0(t)}$$

which proves that the dynamic equation derived is equivalent to the steady state equation as reported by Sacoto (1999). A generic dilution step model is shown below and is similar in structure to equation (6.2)

$$\frac{d(C_i)}{dt} = \frac{q_{i-1}(t)}{V_i} C_{i-1}(t) - \frac{(Q_i(t) + q_{i-1}(t))}{V_i} C_i(t) \quad (6.4)$$

where i is the dilution step.

6.2.3 Implementation

The CSDS prototype has been implemented as depicted in Figure 6.2. There are four main parts to the system: the sampling system, the pumping system, the tubing

network, and the sensor. Each of these sections may be modified depending on the application though for this discussion the most applicable scheme developed at the University of South Florida is implemented.

The reactor sampling is carried out by a sample recycle stream from which a sample is taken and sent to the CSDS. The most important design features here are the tubing selection and pump speed which must be chosen to minimize the sample and prevent clogging.

There are two different pumps used to operate the dilution system: sample pumps and dilution pumps. Both pumps use the same model pump heads and drivers; peristaltic quick load made by Cole-Parmer (Model: 7021-24) and a modular drive by Cole-Parmer (Model 7553-70) respectively. The advantage to using two separate pumps is that the dilution ratio can be varied greatly because the sample and dilution lines can be manipulated independently of one another.

The flow rates of the sample and dilution lines depend on the RPMs of the respective pumps and the inner diameter of the tube. Therefore tube diameter is a critical design criterion and the pump's RPMs may be manipulated to maintain a desired concentration of sample in the system. The greater the difference between the inner diameter of the sample line and the inner diameter (ID) of the dilution line, the larger the dilution factor (assuming constant RPM for both the sample and dilution lines). However, the larger the ID of the dilution lines, the more diluent required. Conversely, the smaller the sample line ID, the greater the chance that the line will clog. An optimal design must be developed for the particular application that takes these two factors into account. Some of the other important design features of the CSDS tubing system that are desired include: minimum residence time in the CSDS, minimum sample volume taken

from reactor, avoidance of clogging (caused by high RPMs and small tube diameters), and prevention of temperature gradients.

The tubing material must also be considered as the interaction of the tubing material with the solvent may have possibility to absorb part of the sample on the tubing. For example, in polystyrene latex reactions, styrene adsorbs on the walls of many tubing materials (Sacoto, 1999). Suitable materials must be found depending on the solvent and substance analyzed.

A UV-VIS spectrometer built by Ocean Optics was chosen for this project. The spectrometer measures the absorbance spectra from 190nm to 820nm and was connected to a desktop PC for analysis. A flow through cell was used to interface the spectrometer with the CSDS. The CSDS final dilution stream is connected to the this cell and the spectroscopic analysis is performed continuously.

6.3 Automation and Control of the CSDS

The main purpose of the CSDS is to dilute the product so that the absorbance, *i.e.* concentration, is within a specified window so spectroscopic analysis can be performed on the sample. In this system, the sample pump's rpm is kept at a constant rate; thus changing the dilution pump's rpm will alter the dilution ratio, and likewise the absorbance. The automation of the CSDS consists of getting the computer, pumps, and spectrometer communicating with one another in order to produce the correct absorbance.

LabVIEW and National Instruments data acquisition boards are used to interface the dilution system with the computer. Along this line several VIs (virtual instruments) had to be written and developed in LabVIEW to communicate with the pumps and spectrometer and the overall scheme and flow of information are illustrated in Figure 6.3. There were four VIs that had to be developed: the pump, dilution controller, Ocean

Optics (spectrometer), and post-processing VIs. The process begins with the user specifying an absorbance value. The dilution controller calculates a dilution pump voltage based on the equation for a PI controller. This voltage setpoint is passed to the pumps via the pump VI which passes the voltage through the correct channels on the DAQ (data acquisition) board to the pumps. The dilution pump's RPMs change as a function of the new voltage passed to them, thus the concentration (and absorbance) of product changes as shown in equation (6.4). The diluted sample is then passed into the flow through cell where the spectral data is then read from the spectrometer by the Ocean Optics VI and sent to the Post Processing VI. Here the spectral data and dilution ratio are used to calculate the product concentration and absorbance value. The absorbance is sent back to the dilution controller to make any further adjustments.

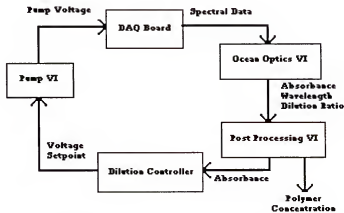


Figure 6.3. Schematic of control scheme in LabVIEW

A PI controller was coded into LabVIEW and is used for the dilution controller.

The proportional and integral parameters were determined by doing a step response and using the ITAE settings and will be explained in greater detail later. In order to help the controller, anti-reset windup was added to the design. There are two parts to this:

installing a maximum upper limit on the error signal sent to the controller and allowing the user to clear out the integral error present as shown by Mattern (1993).

The user interface is shown in Figure 6.4. The user has the ability to specify the absorbance setpoint, change the voltage (RPM) of the sample pumps, change the controller parameters (proportional, integral, and bias), and specify the sample time. The user also has control over the anti-reset windup by changing the upper and lower error limits. The PI controller must first be initialized and then placed in run mode for the system to function properly. Finally, the data can be saved to a spreadsheet if so desired.

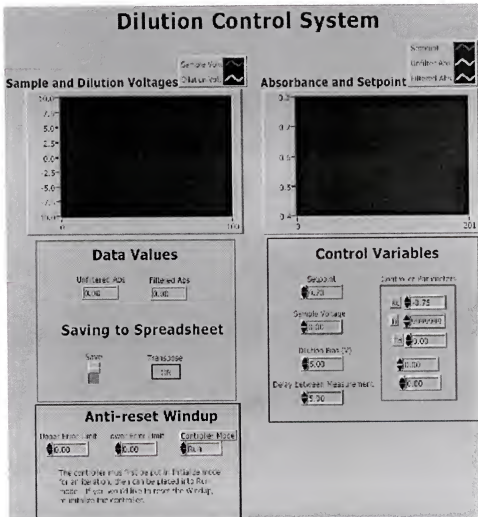


Figure 6.4. User interface for controlling the CSDS in LabVIEW

6.4 Experimental and Simulated Responses of the CSDS

6.4.1 CSDS Open-Loop Response

The CSDS was run in open-loop mode (*i.e.* the controller was turned off) and a step change made in the dilution pump's voltage from 5V to 7V. The absorbance value was recorded as a function of time and the result is illustrated in Figure 6.5. There is a short time delay (θ) of 25s followed by a sharp decrease in absorbance. The increase in voltage to the dilution pump causes the RPMs to increase and likewise the diluent flow rate increases. This rise in diluent flow rate produces a decreased concentration of final sample analyzed in the spectrometer and thus a lower absorbance value.

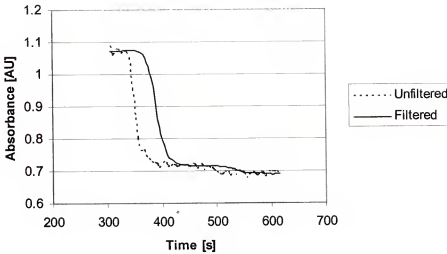


Figure 6.5. Open-loop response of the CSDS to a step change from 5V to 7V in the dilution pump's voltage.

6.4.2 CSDS Closed-Loop Response

Figure 6.5 can be approximated as a first order plus time delay (FODT) system and the parameters K , θ , and τ can be easily determined from such experimental response data (Seborg *et. al.*, 1989) where K is the gain, θ is the time delay, and τ is the time constant. One approach to developing controller relationships is based on a performance

index that takes into account the entire closed-loop system. The integral of the time-weighted absolute error (ITAE) is one method based on the equation

$$ITAE = \int_0^{\infty} t|e(t)|dt$$

where PI controller correlations have been developed that minimize this error. The ITAE formula penalizes errors that endure for long periods of time and preferred over other methods because it results in conservative controller settings. For this project, the type of input considered was a set point change which results in the following equations for a PI controller

$$KK_c = 0.586(\theta / \tau)^{-0.916}$$

$$\tau / \tau_i = 1.03 - 0.165(\theta / \tau)$$

where K_c is the controller gain and τ_i is the integral time. Using the step response in Figure 6.5 the following values for controller parameters were calculated

$$K_c = -3.55 \quad \tau_i = 33.6s$$

It is worth noting that the gain of the controller is negative because this is an inverse response system meaning that an increase in the diluent flow rate will decrease the absorbance (concentration) of the final sample.

Phenol red solution combined with a buffer solution (pH 7.4) was used to test the dilution system. The sample pump's rpms were kept at a constant level (100 rpm) in order to create a constant sample environment. The ITAE tuning parameters were entered into the system via the user interface in LabVIEW. The controller was initialized and a step change was made in the absorbance from 0.7AU to 0.9AU. In Figure 6.6 the closed-

loop response of the CSDS is illustrated. The system reaches the new steady state set point in less than 4 minutes and produces a stable, smooth response.

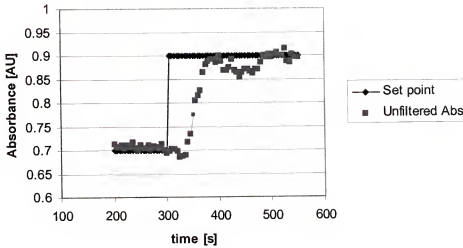


Figure 6.6. Closed-loop response of absorbance with ITAE tuning parameters

The response of the input (dilution voltage) to the CSDS was also recorded versus time and is shown in Figure 6.7. The voltage begins at roughly 7.5V and decreases sharply to a value around 6V. The voltage decreases because the set point of the absorbance increases and the CSDS is an inverse response system.

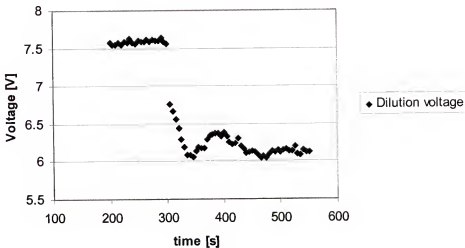


Figure 6.7. Closed-loop response of dilution voltage (input) with ITAE tuning parameters

6.4.3 CSDS Simulation

The dynamic model of the dilution system was coded into Matlab and Simulink and a S-function written in Matlab entitled `csds_control.m` and is shown in Figure 6.8. `Csds_control` contains the differential equations from the dynamic model that are responsible for calculating the changes in concentration (absorbance) for each dilution step. Transport delays are also included in the model, but are currently static delays despite the fact that the RPMS of the pump will vary causing changing time delays.

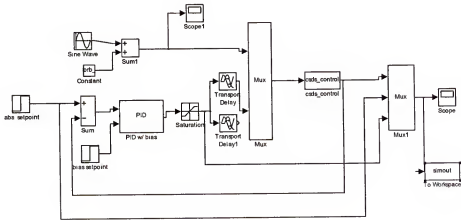


Figure 6.8. Diagram of the Simulink model used for simulations

A model for the relationship between the pump speed and time delay must be established in order to be used in MATLAB and Simulink. A simple linear model was proposed to model the pumps and the parameters estimated using graphs similar to that illustrated in Figure 6.9. Each line, dilution and sample has its own corresponding equation that is used to model the pump.

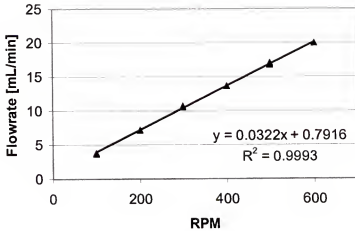


Figure 6.9. Example of pump calibration curve used for CSDS simulation

The models for the dilution and sample pumps were obtained and coded into MATLAB. A simulation of the CSDS was performed using the same exact set point change and controller parameters as discussed in section 6.4.2. As seen in Figure 6.10, the simulated response agrees reasonably well with the experimental data. Both of the responses exhibit the same time delay and have similar rise times.

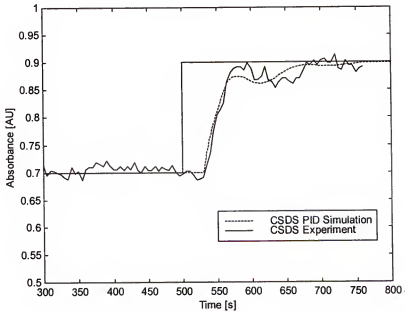


Figure 6.10. Theoretical and experimental responses of first dilution step to setpoint change

The oscillatory nature of the two responses exhibit the same trends, yet have distinct differences. For example the simulated response leads the experimental response both in rise time and in the changes in oscillation. This difference could be due in part to the static time delay used in the simulation while the experimental system has a dynamic time delay.

Further agreement can be seen in Figure 6.11 that compares the theoretical and experimental dilution pump responses. The shapes of the two curves are almost identical being only slightly offset from one another. The encouraging aspect is that the slopes are the same for the entire time frame involved.

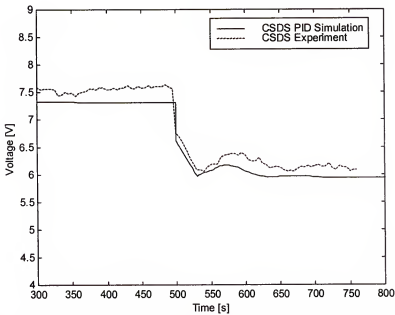


Figure 6.11. Theoretical and experimental dilution voltage responses

6.5 Conclusions and Future Work

There are several places in the dilution system where more work needs to be done. First, a flowmeter must be installed and verified which will provide more accurate models for the pumps in terms of both transient and steady-state behavior. These more accurate models will aid both experimental and theoretical work by improving controller tuning

parameters. The most important aspect of the flowmeter, however, will be the added ability to measure the dilution ratio instead of using models to calculate it. This will lead to a more accurate determination of the concentration.

As more dilution steps are added, the time delay will increase. A more advanced control scheme, such as a Smith predictor or predictive control, may be necessary. It is believed that a Smith predictor or predictive control scheme would greatly enhance the ability of the controller to react to both disturbances and changes in set point.

CHAPTER 7 CONCLUSIONS AND FUTURE WORK

7.1 Conclusions

This dissertation presents an in-depth exploration of theoretical robust control as well as the design and implementation of subsystems for an emulsion polymerization reactor.

Chapters 2 through 4 investigate theoretical process control challenges, specifically theoretical robust control and disturbance predictive control. Chapter 2 presents a revised scheme of the critical direction theory that is now applicable to nonlinear, non-convex systems. In addition, analytical expressions are determined for the minimizing amplitude for a variety of nonlinear systems. Chapter 3 analyzes the robustness of predictive controllers using the parametric stability margin. In particular, a systematic algorithm is developed that finds predictive controller tuning parameters that make the controller robustly stable for a given uncertainty. Chapter 4 develops a disturbance predictive control law that is applicable to systems that have large disturbances present such as a wastewater treatment plant. It was shown that for linear plants this control law does an excellent job of disturbance rejection but performs poorly for highly nonlinear plants.

Chapter 5 discusses the addition of an excess volume model to conversion calculations. The excess volume model increases the numerical complexity of the analysis but greatly improves the conversion calculations for a variety of systems. However, the numerical issues were analyzed and a solution obtained. Finally, Chapter 6

extends the work on the CSDS that was begun at the University of South Florida. The CSDS was automated and controlled via LabVIEW and a dynamic model was developed for the system. The control scheme implemented keeps the absorbance value of the sample at a specified threshold required for spectroscopic measurements.

7.2 Future Work

The nonlinear Nyquist robust stability margin developed in Chapter 2 needs to be applied to relay based PI controllers and perhaps extended to include controller synthesis. Another area of research interest is the stability analysis of infinite horizon predictive controllers developed by Cannon and Kouvaritakis (2000). Work is currently proceeding on developing the algorithms involved and determining if the infinite horizon increases or decreases the robustness of the controller. The disturbance predictive controller developed in Chapter 3 must be modified so it is effective for nonlinear systems. This could be done through an adaptive control scheme or more effectively through the use of a nonlinear disturbance predictive controller.

Finally the subsystems developed in Chapters 5 and 6 need to be implemented on an emulsion polymerization reactor. In conjunction with a multi-angle, multi-wavelength spectrometer the particle size distribution can be obtained on-line. Significant advances in the control of the particle size will be possible once the test bed is implemented.

APPENDIX A
PROOF OF EQUATION (5.15)

Proof. The following proof is derived using root analysis for a cubic equation.

The general form of any cubic equation is

$$z^3 + a_2 z^2 + a_1 z + a_0 = 0$$

and define q and r as

$$q = \frac{1}{3}a_1 - \frac{1}{9}a_2^2 \quad (\text{A.1})$$

$$r = \frac{1}{6}(a_1 a_2 - 3a_0) - \frac{1}{27}a_2^3 \quad (\text{A.2})$$

It can be shown that if

$$D = q^3 + r^2 > 0 \quad (\text{A.3})$$

there is one real root and two complex conjugate roots. The cubic equation for conversion using the Redlich-Kister model is

$$x^3 + \left(-\frac{3B-A}{2B}\right)x^2 + \left(-\frac{A+v_{100\%}-v_{0\%}-B}{2B}\right)x + \left(-\frac{v_{0\%}-v(x)}{2B}\right) = 0$$

and using equations (A.1), (A.2), and (A.3) the discriminant D becomes

$$D = -\frac{1}{46656} \frac{(6Bv_{100\%} - 6Bv_{0\%} + B^2 + A^2)^3}{B^6} + \left[\frac{(3B-A)}{24B^2} (A + v_{100\%} - v_{0\%} - B) + \frac{v_{0\%} - v(x)}{4B} + \frac{(3B-A)^3}{216B^3} \right]^2 \quad (\text{A.4})$$

The issue in determining if $D > 0$ involves analyzing the cubic term in (A.4) to see if it is positive or negative. Therefore, define

$$6Bv_{100\%} - 6Bv_{0\%} + B^2 + A^2 < 0$$

and rearrange to yield

$$\frac{A^2 + B^2}{6B} < v_{0\%} - v_{100\%}$$

The above equation matches equation (5.15) and the proof is concluded.

LIST OF REFERENCES

- Baab, C. T., Cockburn, J. C., Latchman, H. A., and Crisalle, O. D. (2001). "Extension of the Nyquist robust stability margin to systems with nonconvex values sets," *Proceedings of the American Control Conference*, Washington, D.C., pp. 1414-1419, IEEE, Piscataway, NJ.
- Belfonte, G., B. Bona, and V. Cerone (1990). "Parametric estimation algorithms for a set-membership description of uncertainty," *Automatica*, Vol, 26, No. 5, pp. 887-898.
- Bhattacharyya, S. P., H. Chapellat, and L. H. Keel, *Robust Control The Parametric Approach*, Prentice Hall, Upper Saddle River, NJ (1995).
- Bhattacharyya, S., L.H. Keel, and S.P. Bhattacharyya (1993). "Robust stabilizer synthesis for interval plants using H -infinity methods," *Proceedings of Conference on Decision and Control*, San Antonio, Texas, pp. 3003-3008.
- Bierck, Barnes R., Blatchley, III, Ernest R., Connell, Gerald F., Cudrak, Audrey A., Devkota, Laxman Mani, Finch, Gordon R., Fleury, Michael, Hart, Frederick L., Hom, Victor, Jeyanayagam, Samuel S., Kinner, Nancy E., and Scheible, Otto K. (1996) *Wastewater Disinfection, Manual of Practice FD-10*, Water Environment Federation, Alexandria, VA.
- Blackley, D. C. (1975). *Emulsion Polymerization: Theory and Practice*, John Wiley & Sons, New York.
- Canegallo, S., Carra, S., Morbidelli, M., and Guisepppe, S. (1993). "Densimetry for on-line conversion monitoring in emulsion homo- and copolymerization," *Journal of Applied Polymer Science*, Vol. 47.
- Cannon, M. and Kouvaritakis, B. (2000). "Infinite horizon predictive control of constrained continuous-time linear systems," *Automatica*, Vol. 36, pp. 943-955.
- Clarke, D. W., C. Mohtadi, and P. S. Tuffs (1987). "Generalized predictive control: parts I and II," *Automatica*, Vol. 23, No. 2, pp. 137-160.
- Crisalle, O. D., D. E. Seborg, and D. A. Mellichamp (1989). "Theoretical analysis of long-range predictive controllers," *Proceedings of the American Control Conference*, Pittsburg, PA.
- Demir, F. (2001) "Modeling of chlorine disinfection and kaolin dispersion systems with control applications," Doctoral Dissertation, University of Florida, Gainesville, FL.

- Doyle, J.C. (1982). "Analysis of feedback systems with structured uncertainties," *IEE Proceedings Part D*, vol. 129, pp. 242-250.
- Doyle, J. C. (1983). "Synthesis of robust controllers and filters," *Proceedings of the 22nd IEEE Conference on Decision and Control*, pp. 109-114.
- Doyle, J. C., Glover, K., Khargonekar, P. P., and Francis, B. A. (1989). "State space solution to standard H_2 and H_∞ control problems," *IEEE Transactions on Automatic Control*, vol. 34, no. 8, pp. 831-847.
- Doyle, J.C., B.A. Francis and A.R. Tannenbaum (1992). *Feedback Control Theory*, Macmillan Publishing Company, New York.
- Elicabe, G. and Garcia-Rubio, L.H. (1988). "Latex particle size distribution from turbidity using inversion techniques," *Journal of Colloid and Interfacial Science*, vol 129.
- Elicabe, G. and Garcia-Rubio, L.H. (1990). "Approximations to the refractive index for light scattering measurements," *Internal Report for Center for Materials Development*, University of South Florida.
- Francis, B. A. and Zames, G. (1984). "On H_∞ - optimal sensitivity theory for SISO feedback systems," *IEEE Transactions on Automatic Control*, vol. 29, no. 1, pp. 9-16
- Genceli, H. and M. Nikolaou (1993). "Robust stability analysis of constrained ℓ_1 -norm model predictive control," *AIChE Journal*, Vol. 39, No. 12., pp. 2098-2107.
- Gilbert, R. G. (1995). *Emulsion Polymerization: A Mechanistic Approach*, Academic Press, London.
- Guinot, P. (2000). "On-line monitoring of emulsion copolymerization using hardware sensors and calorimetry," *Journal of Polymer Reaction Engineering*, Vol. 8.
- Guzzella, L., O.D. Crisalle, F. Kraus and D. Bonvin (1991). "Necessary and sufficient conditions for the robust stabilizing control of linear plants with ellipsoidal parametric uncertainties," *Proceeding of Conference on Decision and Control*, Brighton, U.K., pp. 2948-2953.
- Hammer, Mark J., and Hammer, Jr., Mark J. (1996). *Water and Wastewater Technology*, 3rd Edition, Prentice Hall Inc., Englewood Cliffs, NJ.
- Chrissagis, K., O. D. Crisalle, and M. Sznajder (1996). "Robust unconstrained predictive control design with guaranteed nominal performance," *AIChE Journal*, Vol. 42, No. 5, pp. 1293-1303.

- Jolley, Robert L., Condie, Lyman W., Johnson, J. Donald, Katz, Sidney, Minear, Roger A., Mattice, Jack S., and Jacons, Vivian A., editors (1990). *Water Chlorination Chemistry, Environmental Impact and Health Effects*, vol. 6, Lewis Publishers, Inc., Chelsea, MI.
- Khalil, H.K. (1992), *Nonlinear Systems*, Macmillan Publishing Company, New York.
- Kharitonov, V. L. (1979). "Asymptotic stability of an equilibrium position of a family of systems of linear differential equations," *Differential Equations*, vol. 14, pp. 1483-1485.
- Kourti, M., Penlidis, A., MacGregor, J. F., and Hamielec, A. E. (1984). *Particle Size Distribution, Assessment, and Characterization*, 242, ACS Symposium Series.
- Kouvaritakis, B., Rossiter J. A., and A. Chang (1992). "Stable generalized predictive control: an algorithm with guaranteed stability," *IEEE Proceedings – Part D*, Vol. 139, pp. 349-363.
- Landau, Y. D. (1998). *Adaptive Control*, Springer Publishing, New York.
- Latchman, H. A. and Crisalle, O. D. (1995). "Exact robustness analysis for highly structured frequency-domain uncertainties," *Proceedings of the American Control Conference*, Seattle, WA, pp. 3982-3987, IEEE, Piscataway, NJ.
- Latchman, H. A., Crisalle, O. D., and Basker, V. R. (1997). "The Nyquist robust stability margin – a new metric for robust stability," *International Journal of Robust and Nonlinear Control*, vol. 7, pp. 211-226.
- Leigh, J.R. (1983), *Essentials of Nonlinear Control Theory*, Peter Peregrinus Ltd., London, U.K..
- Mahon, H. M., C. T. Baab, O. D. Crisalle (1999). "On a quasi-convex method for designing robust predictive controllers," *Proceedings of the American Control Conference*, San Diego, CA.
- Mattern, D. (1993). "A comparison of two multi-variable integrator windup protection schemes," *NASA Contractor Report*, Washington D.C.
- Meredith, C. (2003). "Wastewater chlorination, run-to-run, and stream neutralization strategies," Doctoral Dissertation, University of Florida, Gainesville, FL.
- Metcalf & Eddy, Inc. (1979) *Wastewater Engineering: Treatment Disposal Reuse*, 2nd Edition. McGraw-Hill, New York, NY.
- Mohler, R.R. (1991). *Nonlinear Systems Volume I: Dynamics and Control*, Prentice Hall, Englewood Cliffs, New Jersey.

- Morris, J. C., and Wei, I. W. (1969). "Chlorine ammonia breakpoint reactions: model mechanisms and computer simulation," *American Chemical Society*, Minneapolis, MN.
- Moritz, H. U., Taylor, T. W., and Reichert, K. H. (1985). "Kinetic studies of steric stabilized emulsion polymerization of vinyl acetate," *Proceedings from ACS Division of Polymeric Material*, Washington, D.C.
- Nicoli, D. F., and Elings, V. B. (1989). US Patent 4794806.
- Nunes, G. C., S. Kincal, and O. D. Crisalle (2003). "A polynomial perspective on the stability of multivariable predictive controllers," *Computers and Chemical Engineering*.
- Nyquist, H. (1932). "Regeneration theory," *Bell Systems Technical Journal*, vol. 11, pp. 126-147.
- Ogunnaike, Babatunde A. and Ray, W. Harmon (1994). *Process Dynamics, Modeling, and Control*. Oxford University Press, New York, NY.
- Ponnuswamy, S. and Shah, S. L. (1986). "On-line monitoring of polymer quality in a batch polymerization reactor," *Journal of Polymer Science*, Vol 32.
- Sacoto, P. (1996). Undergraduate Research Project Report, University of South Florida, submitted to the ERC on Particle Science and Technology, University of Florida.
- Sacoto, P. (1999). "Continuous sampling and dilution system for the characterization of concentrated dispersions," Master's Thesis, Department of Chemical Engineering, University of South Florida.
- Safonov, M. G. (1982). "Stability margins of diagonally perturbed multivariable feedback systems," *IEE Proceedings Part D*, 129, pp. 251-256.
- Safonov M. G., and Verma, M. S. (1985). " l_{∞} optimization and Hankel approximations," *IEEE Transactions on Automatic Control*, vol. 30, no. 3, pp. 279-280.
- Schork, F. J. and Ray, W. H. (1980). "On-line monitoring of emulsion polymerization reactor dynamics," *Journal of the American Chemical Society Division of Organic Coatings and Plastics Chemistry*, Vol. 43.
- Schork, F. J. (1981). "The dynamics of continuous emulsion polymerization reactors," Doctoral Dissertation, University of Wisconsin-Madison, Madison, WI

- Schork, F. J. and Ray, W. H. (1983). "On-line measurement of surface tension and density with application to emulsion polymerization," *Journal of Applied Polymer Science*, Vol. 28.
- Schork, F. J. and Ray, W. H. (1987). "The dynamics of continuous emulsion polymerization of methylmethacrylate," *Journal of Applied Polymer Science*, Vol. 34.
- Seborg, D. E., Edgar, T. F., and Mellichamp, D. A. (1989). *Process Dynamics and Control*. John Wiley & Sons, New York.
- Smith, R. (1971). "Wastewater treatment plant control," Environmental Protection Agency, PB 213 827.
- Snoeyink, V. L., and Jenkins, D. (1980). *Water Chemistry*, John Wiley & Sons, New York, NY.
- Vara, J. M. (2000). "Development of instrumentation for on-line monitoring of emulsion polymerization reactors," Master's Thesis, University of South Florida, Tampa, FL.
- White, L. B. (1994). US Patent 5297431.
- Zafirou, E. (1990). "Robust model predictive control of processes with hard constraints," *Computers Chem. Engin.*, Vol. 14, No. 4, pp. 359-371.
- Zames, G. (1981). "Feedback and optimal sensitivity: Model reference transformation, multiplicative seminorms, and approximate inverses," *IEEE Transactions on Automatic Control*, vol. 34, no. 2, pp. 301-320.

BIOGRAPHICAL SKETCH

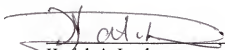
Brian Joseph Remark was born in Richland, Washington, on September 22, 1976. He graduated with a B.S. in chemical engineering from the Georgia Institute of Technology in June 1998. Mr. Remark joined the graduate program at the University of Florida in August 1998. He received his Ph.D. in chemical engineering in May 2004.

I certify that I have read this study and that in my opinion it conforms to acceptable standards of scholarly presentation and is fully adequate, in scope and quality, as a dissertation for the degree of Doctor of Philosophy.



Oscar D. Crisalle, Chairman
Associate Professor of Chemical
Engineering

I certify that I have read this study and that in my opinion it conforms to acceptable standards of scholarly presentation and is fully adequate, in scope and quality, as a dissertation for the degree of Doctor of Philosophy.



Hariph A. Latchman
Professor of Electrical and Computer
Engineering

I certify that I have read this study and that in my opinion it conforms to acceptable standards of scholarly presentation and is fully adequate, in scope and quality, as a dissertation for the degree of Doctor of Philosophy.



Jason F. Weaver
Assistant Professor of Chemical
Engineering

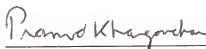
I certify that I have read this study and that in my opinion it conforms to acceptable standards of scholarly presentation and is fully adequate, in scope and quality, as a dissertation for the degree of Doctor of Philosophy.



Richard B. Dickinson
Associate Professor of Chemical
Engineering

This dissertation was submitted to the Graduate Faculty of the College of Engineering and to the Graduate School and was accepted as partial fulfillment of the requirements for the degree of Doctor of Philosophy.

May 2004

A handwritten signature in dark ink, reading "Pramod Khargonekar", written over a horizontal line.

Pramod Khargonekar
Dean, College of Engineering

Winfred M. Phillips
Dean, Graduate School